



# 1 Impact of HO<sub>2</sub>/RO<sub>2</sub> ratio on highly oxygenated α-pinene 2 photooxidation products and secondary organic aerosol formation 3 potential

4 Yarê Baker<sup>1</sup>, Sungah Kang<sup>1</sup>, Hui Wang<sup>1</sup>, Rongrong Wu<sup>1</sup>, Jian Xu<sup>1</sup>, Annika Zanders<sup>1</sup>, Quanfu He<sup>1</sup>,  
5 Thorsten Hohaus<sup>1</sup>, Till Ziehm<sup>1</sup>, Veronica Geretti<sup>2</sup>, Thomas J. Bannan<sup>3</sup>, Simon P. O'Meara<sup>3,4</sup>, Aristeidis  
6 Voliotis<sup>3</sup>, Mattias Hallquist<sup>2</sup>, Gordon McFiggans<sup>3</sup>, Sören R. Zorn<sup>1</sup>, Andreas Wahner<sup>1</sup>, and Thomas F.  
7 Mentel<sup>1</sup>

8 <sup>1</sup>Institute for Energy and Climate Research, IEK-8, Forschungszentrum Jülich, 52425 Jülich, Germany

9 <sup>2</sup>Atmospheric Science, Dept. of Chemistry, University of Gothenburg, Gothenburg, 412 96, Sweden

10 <sup>3</sup>Department for Earth and Environmental Sciences, University of Manchester, Manchester, M13 9PL, UK

11 <sup>4</sup>National Centre for Atmospheric Science, University of Manchester, Manchester, M13 9PL, UK

12

13 *Correspondence to:* Thomas F. Mentel (t.mentel@fz-juelich.de)

14 **Abstract.** Highly oxygenated molecules (HOM) from the atmospheric oxidation of biogenic volatile organic compounds are  
15 important contributors to secondary organic aerosol (SOA). Organic peroxy radicals (RO<sub>2</sub>) and hydroperoxy radicals (HO<sub>2</sub>)  
16 are key species influencing the HOM product distribution. In laboratory studies experimental requirements often result in  
17 overemphasis of RO<sub>2</sub> cross-reactions compared to reactions of RO<sub>2</sub> with HO<sub>2</sub>. We analyzed the photochemical formation of  
18 HOMs from α-pinene and their potential to contribute to SOA formation under high (≈1/1) and low (≈1/100) HO<sub>2</sub>/RO<sub>2</sub>  
19 conditions. As HO<sub>2</sub>/RO<sub>2</sub> > 1 is prevalent in the daytime atmosphere, sufficiently high HO<sub>2</sub>/RO<sub>2</sub> is crucial to mimic  
20 atmospheric conditions and to prevent biases by low HO<sub>2</sub>/RO<sub>2</sub> on the HOM product distribution and thus SOA yield.  
21 Experiments were performed under steady-state conditions in the new, continuously stirred tank reactor SAPHIR-STAR at  
22 Forschungszentrum Jülich. The HO<sub>2</sub>/RO<sub>2</sub> ratio was increased by adding CO, while keeping the OH concentration constant.  
23 We determined the HOM's SOA formation potential, considering their fraction remaining in the gas phase after seeding with  
24 (NH<sub>4</sub>)<sub>2</sub>SO<sub>4</sub> aerosol. Increase of HO<sub>2</sub>/RO<sub>2</sub> led to a reduction in SOA formation potential, with the main driver being a ≈60%  
25 reduction in HOM-accretion products. We also observed a shift in HOM-monomer functionalization from carbonyl to  
26 hydroperoxide groups. We determined a reduction of the HOM's SOA formation potential by ≈30% at HO<sub>2</sub>/RO<sub>2</sub>≈1/1.  
27 Particle phase observations measured an about according decrease in SOA mass and yield. Our study showed that too low  
28 HO<sub>2</sub>/RO<sub>2</sub> ratios compared to the atmosphere can lead to an overestimation of SOA yields.



## 29 Introduction

30 In the atmosphere highly oxidized products from the oxidation of biogenic or anthropogenic volatile organic compounds  
31 (VOCs) are an important source of secondary organic aerosol (SOA) (Roldin et al., 2019; Mohr et al., 2019). SOA is an  
32 important contributor to the overall ambient aerosol and of interest because of its impact on climate, visibility, and human  
33 health (Hallquist et al., 2009).

34 Recently, many studies (Pullinen et al., 2020; Berndt et al., 2016; Bianchi et al., 2017) have focused on understanding the  
35 oxidation pathways of VOCs that yield highly oxygenated molecules (HOMs), as these are expected to be of low enough  
36 volatility to condense into the particle phase. One important tool for the investigation of VOC degradation and SOA  
37 formation is the utilization of experiments in atmospheric simulation chambers (Hidy, 2019). Such experiments have also  
38 helped to elucidate key processes in the HOM formation, i.e. the process of autoxidation.

39 After an initial oxidant attack and the formation of a peroxy radical ( $\text{RO}_2$ ), autoxidation adds oxygen to the molecule via an  
40 internal H-shift to the peroxy group, forming a hydroxy peroxide group and an alkyl radical, to which  $\text{O}_2$  immediately adds,  
41 reestablishing the peroxy functionality. This process can be repeated multiple times yielding almost instantaneously highly  
42 oxygenated peroxy radicals ( $\text{HOM-RO}_2$ ) which are terminated to a series of HOM closed-shell products (Bianchi et al.,  
43 2019; Ehn et al., 2014; Crouse et al., 2013).

44 Chamber studies often work with a singular compound and operate at higher precursor concentrations than those observed in  
45 the atmosphere for experimental reasons. These experiments cannot represent the complex mixture of VOCs and oxidized  
46 VOCs present in the atmosphere (McFiggans et al., 2019). Higher precursor concentrations can lead per se to higher SOA  
47 yields than observed in the atmosphere (a well characterized phenomenon (see Henry et al. (2012), Shilling et al. (2009)) and  
48 to a general preference of higher order processes which may not be important in the atmosphere. One example is that  
49 chamber studies tend to overestimate the role of cross reactions between organic peroxy radicals ( $\text{RO}_2$ ) owing to high  
50 precursor concentrations of a single VOC. In chambers, reactions of  $\text{HOM-RO}_2$  with other organic peroxy radicals terminate  
51 the autoxidation chain, leading typically to multifunctional carbonyl and alcohol compounds. In comparison, in the  
52 atmosphere termination by  $\text{HO}_2$  is more likely, leading to multifunctional hydroperoxides. In presence of sufficient  $\text{NO}$ ,  
53 termination to multifunctional organic nitrates may be more important (Schervish and Donahue, 2021).

54 Another possible termination reaction of  $\text{HOM-RO}_2$  with  $\text{HOM-RO}_2$  and less oxidized  $\text{RO}_2$  leads to the formation of  
55 accretion products, which are expected to be extremely low volatile organic compounds (ELVOCs) and are therefore  
56 expected to contribute to new particle formation and SOA formation (Ehn et al., 2014; Berndt et al., 2018). Schervish and  
57 Donahue (2021) raised awareness that chamber studies could overestimate the SOA formation potential from the oxidation  
58 of terpenes such as  $\alpha$ -pinene compared to the atmosphere, because of missing  $\text{HO}_2$  and small  $\text{RO}_2$  (e.g.  $\text{CH}_3\text{O}_2$ ), which favors  
59 accretion product formation.



60 In chamber studies the use of higher VOC concentrations is often an unavoidable necessity either to match the sensitivity of  
61 the analytical instrumentation or to overcome chamber related effects. The question remains, how can conditions dictated by  
62 the chamber be steered towards more realistic chemical pathways and higher atmospheric relevance?

63 In this study we address this overestimated importance of peroxy radical cross reactions. We studied the photooxidation of  $\alpha$ -  
64 pinene in a series of steady-state experiments in the newly built continuously stirred tank reactor SAPHIR-STAR (a  
65 modernized version of JPAC, see Mentel et al. (2009)).

66 In these experiments, after an initial  $\alpha$ -pinene photooxidation phase as a reference, CO was added to the oxidation system to  
67 represent small, oxidized VOCs in the atmosphere that can produce HO<sub>2</sub> by reaction with OH (compare Schervish and  
68 Donahue (2021)). Presence of CO shifts the HO<sub>2</sub> to RO<sub>2</sub> ratio, increasing the importance of the RO<sub>2</sub> termination with HO<sub>2</sub>.  
69 However, McFiggans et al. (2019) showed that one limiting factor in mixture experiments is oxidant scavenging: the  
70 products and their yields in mixed systems change, because there is less OH available to the individual VOC. Thus, after the  
71 CO addition the OH production in the chamber was increased to compensate for the oxidant scavenging. The OH levels in  
72 the system before and after the CO addition were approximately the same, keeping the  $\alpha$ -pinene OH turnover, as well as the  
73 primary peroxy radical production approximately constant.

74 Furthermore, the addition of seed particles ((NH<sub>4</sub>)<sub>2</sub>SO<sub>4</sub>) allowed us to observe the condensation behavior of the HOM-  
75 products and to compare our gas phase observations directly with particulate phase measurements of the condensed organic  
76 mass.

77 In this study we will address two central questions: How does the shift in HO<sub>2</sub>/RO<sub>2</sub> impact the oxidation mechanism of  
78  $\alpha$ -pinene, especially the HOM formation pathway? And what is the subsequent impact on the SOA formation potential of the  
79  $\alpha$ -pinene photooxidation system? As the central analysis tool, we will use high resolution time of flight mass spectrometry  
80 with chemical ionization (HR-TOF-CIMS).

## 81 **1 Methods**

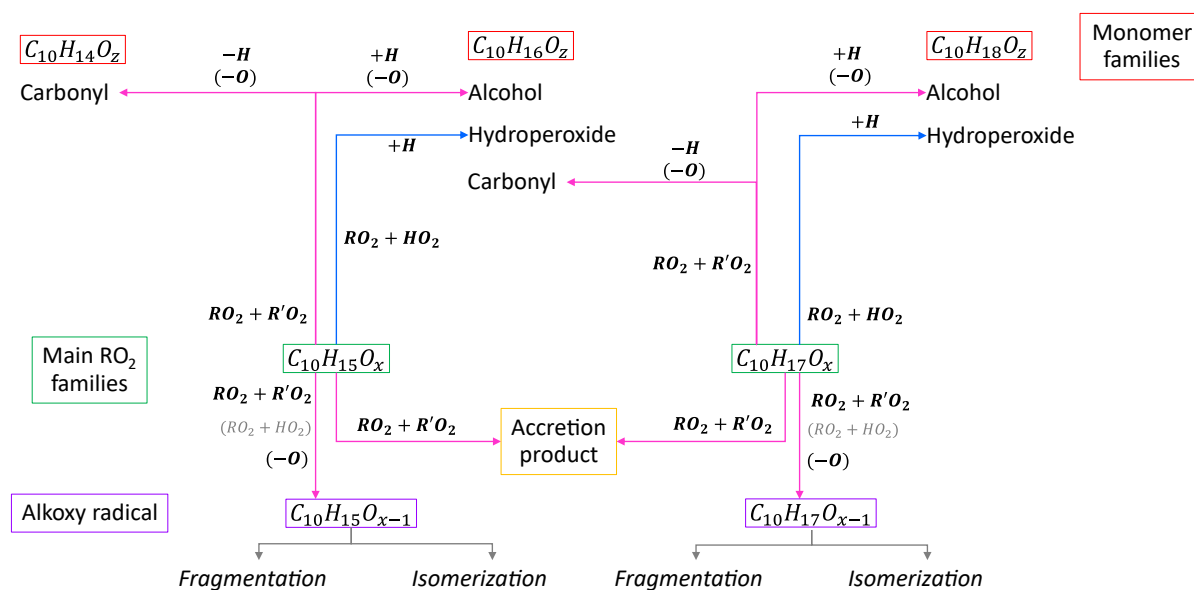
### 82 **1.1 Generic $\alpha$ -pinene HOM peroxy radical chemistry**

83 The chemical mechanistic information for the basic oxidation scheme of  $\alpha$ -pinene was taken from the Master Chemical  
84 Mechanism MCM v3.3.1 (Jenkin et al., 1997; Saunders et al., 2003) (<http://mcm.york.ac.uk>). The main peroxy radicals  
85 expected from  $\alpha$ -pinene photooxidation are C<sub>10</sub>H<sub>17</sub>O<sub>x</sub> and C<sub>10</sub>H<sub>15</sub>O<sub>x</sub>. C<sub>10</sub>H<sub>17</sub>O<sub>x</sub> is formed by the addition of OH to  $\alpha$ -pinene,  
86 followed by O<sub>2</sub> (starting RO<sub>2</sub>: C<sub>10</sub>H<sub>17</sub>O<sub>3</sub>) (MCM v3.3.1 (Jenkin et al., 1997; Saunders et al., 2003)). Studies showed that the  
87 autoxidation can start from C<sub>10</sub>H<sub>17</sub>O<sub>3</sub> with the four-member ring in  $\alpha$ -pinene opened (Berndt, 2021; Xu et al., 2019).

88 For C<sub>10</sub>H<sub>15</sub>O<sub>x</sub> the autoxidation chain is assumed to start with C<sub>10</sub>H<sub>15</sub>O<sub>4</sub>, which can be formed directly from ozonolysis via the  
89 vinyl hydroperoxide path (Johnson and Marston, 2008; Iyer et al., 2021) or via H-abstraction from first-generation oxidation



90 products such as pinonaldehyde ( $C_{10}H_{16}O_2$ ). (MCM v3.3.1 (Jenkin et al., 1997; Saunders et al., 2003; Fantechi et al., 2002).  
 91 A recent study suggests direct H-abstraction by OH from  $\alpha$ -pinene (Shen et al., 2022).  
 92 The autoxidation process is rapid with H-shift rates of about  $0.01 - 0.1 \text{ s}^{-1}$  and faster (Piletic and Kleindienst, 2022; Berndt,  
 93 2021; Xu et al., 2019; Vereecken et al., 2007). Once the autoxidation process starts it quickly adds more oxygen to the  
 94 molecule, until the difficulty in abstracting remaining H-atoms slows down the reaction sufficiently such that termination  
 95 reactions can compete. In the absence of  $NO_x$ , the peroxy radicals have two major bimolecular termination channels: the  
 96 reaction with another  $RO_2$  or with  $HO_2$ . A third pathway is the intramolecular termination (Rissanen et al., 2014).  
 97 Based on the considerations above, we apply a simplified generic reaction scheme to analyze our observations. **Figure 1**  
 98 shows an overview of the reaction pathways for the main peroxy radical families in the  $\alpha$ -pinene photooxidation and the  
 99 resulting product groups and families. The compounds can be separated into four classes; peroxy radicals (HOM- $RO_2$ ),  
 100 monomers (HOM-Mon), accretion products (HOM-Acc) and fragments (HOM-Frag). The HOM- $RO_2$  class consists of all  
 101 detected HOM- $RO_2$ , with special focus on the analysis of the  $C_{10}$  HOM- $RO_2$  family. The HOM-Mon class contains the  
 102 closed-shell HOM- $C_{10}$  products. The compounds in the fragment class contain less than ten carbon atoms, while all  
 103 HOM-Acc compounds contain more than ten carbon atoms. The compound classes are further divided into groups and  
 104 families. Here, the term group is used for compounds with the same carbon number, while a family contains all compounds  
 105 with the same carbon and hydrogen number but a varying oxygen number.



106

107 **Figure 1: Overview of important reaction pathways of  $\alpha$ -pinene  $RO_2$  with other  $RO_2$  and  $HO_2$ .**



108 The termination of  $\text{RO}_2$  with  $\text{HO}_2$  will lead to hydroperoxide formation:



109 In the case of  $\text{C}_{10}\text{H}_{15}\text{O}_x$ , reaction (**R1**) will lead to multifunctional  $\text{C}_{10}\text{H}_{16}\text{O}_z$  hydroperoxides (wherein the notation  
110 “hydroperoxides” or “carbonyls”, “alcohols” etc. here and in the following relates to the functionality of the group formed by  
111 the termination reaction). For  $\text{C}_{10}\text{H}_{17}\text{O}_x$  it will lead to the formation of  $\text{C}_{10}\text{H}_{18}\text{O}_z$  hydroperoxides. The termination via  
112  $\text{RO}_2 + \text{RO}_2$  can either result in the formation of accretion products or in the formation of carbonyls and alcohols. For the  
113 accretion product formation, it is assumed that the two  $\text{RO}_2$  chemically bond eliminating  $\text{O}_2$  from the molecule:



114 Recombination reactions of the main peroxy radical families  $\text{C}_{10}\text{H}_{15}\text{O}_x$  and  $\text{C}_{10}\text{H}_{17}\text{O}_x$  lead to the product families  $\text{C}_{20}\text{H}_{30}\text{O}_z$   
115 (combination of two  $\text{C}_{10}\text{H}_{15}\text{O}_x$ ),  $\text{C}_{20}\text{H}_{32}\text{O}_z$  (combination of  $\text{C}_{10}\text{H}_{15}\text{O}_x$  and  $\text{C}_{10}\text{H}_{17}\text{O}_x$ ), and  $\text{C}_{20}\text{H}_{34}\text{O}_z$  (combination of two  
116  $\text{C}_{10}\text{H}_{17}\text{O}_x$ ).

117 However, due to reactions with smaller peroxy radicals, HOM-Acc families with smaller carbon and hydrogen numbers are  
118 also observed. Indeed, one reason why the  $\text{RO}_2 + \text{R}'\text{O}_2$  termination is expected to affect the SOA formation potential is the  
119 formation of accretion products by scavenging of less oxidized and smaller  $\text{RO}_2$  by HOM- $\text{RO}_2$ . Thus, the smaller  $\text{RO}_2$  will  
120 also contribute to the SOA mass which would otherwise not be the case. For the HOM- $\text{RO}_2$  itself, it is expected that they  
121 contribute to SOA formation independently of the termination pathway, due to the low volatility of its expected termination  
122 products (Pullinen et al., 2020; McFiggans et al., 2019).

123 The second  $\text{RO}_2 + \text{R}'\text{O}_2$  termination pathway is the formation of a carbonyl and alcohol compound:



124 In this reaction both radicals lose an oxygen atom, and a hydrogen atom is transferred to the  $\text{RO}_2$  forming the alcohol  
125 termination group. Preferences of  $\text{RO}_2$  to form an alcohol or carbonyl compound are possible for individual reactions, but  
126 statistically carbonyl and alcohols should be formed with the same fractions. Since mass spectrometry can only determine  
127 formula composition, we cannot distinguish alcohols and hydroperoxides, which arise from  $\text{RO}_2$  differing by one O atom.  
128 Therefore, details of balance of alcohol and carbonyl formation cannot be detected.

129 However, the formula composition can help to differentiate certain formation pathways. The  $\text{C}_{10}\text{H}_{14}\text{O}_z$  family contains only  
130 carbonyl formed from a  $\text{C}_{10}\text{H}_{15}\text{O}_x$   $\text{RO}_2$  while the alcohol will be part of the  $\text{C}_{10}\text{H}_{16}\text{O}_z$  family. The  $\text{C}_{10}\text{H}_{16}\text{O}_z$  family also  
131 contains the carbonyl produced from the  $\text{RO}_2 + \text{R}'\text{O}_2$  monomer termination of  $\text{C}_{10}\text{H}_{17}\text{O}_x$ , while the alcohol from this  $\text{RO}_2$   
132 family will be found in the  $\text{C}_{10}\text{H}_{18}\text{O}_z$  family. So, from a diagnostic point of view,  $\text{C}_{10}\text{H}_{14}\text{O}_z$  as well as  $\text{C}_{10}\text{H}_{18}\text{O}_z$  are uniquely  
133 related to a precursor radical family.



134 The classification of the formation pathways of the monomers is helpful to analyze the effect of the HO<sub>2</sub>/RO<sub>2</sub> ratio shift in  
135 the experiments. Considering the termination pathways, a decrease in the C<sub>10</sub>H<sub>14</sub>O<sub>z</sub> family and an increase of the C<sub>10</sub>H<sub>18</sub>O<sub>z</sub>  
136 family is expected with increasing HO<sub>2</sub>/RO<sub>2</sub> because of increasing termination by HO<sub>2</sub> and decreasing termination by RO<sub>2</sub>.  
137 In case of C<sub>10</sub>H<sub>18</sub>O<sub>z</sub> the increase of hydroperoxides is partially compensated by a decrease of the alcohol channel. For  
138 C<sub>10</sub>H<sub>16</sub>O<sub>z</sub> the situation is more complicated as it contains contributions from all termination pathways.

139 Besides closed-shell products, HOM-RO<sub>2</sub> can also form alkoxy radicals (HOM-RO). In general, alkoxy radicals (RO) are  
140 important intermediates in the oxidation scheme of organics and are formed via (**R4**) and probably also via (**R5**) for specific  
141 RO<sub>2</sub> (Jenkin et al., 2019):



142 In reaction (**R5**) OH will be formed. The importance of reaction (**R5**) compared to reaction (**R1**) is still unclear in the  
143 literature, but functionalization of the RO<sub>2</sub> close to the peroxy functionality possibly enables this reaction (Iyer et al., 2018;  
144 Eddingsaas et al., 2012; Hasson et al., 2005; Jenkin et al., 2019). If reaction (**R5**) is of negligible importance, the reaction  
145 scheme will simplify and the effect of increased HO<sub>2</sub>/RO<sub>2</sub> is easier to diagnose.

146 We are interested in the importance of alkoxy radical formation as (HOM)-RO tend to fragment, leading to the formation of  
147 smaller products (Vereecken et al., 2007). In the context of SOA formation, these fragments are less likely to contribute to  
148 SOA mass because of their higher volatility. Since alkoxy radicals are too unstable to be detected directly we use two  
149 diagnosis tools to judge the importance of HOM-RO. Firstly, HOM-RO fragmentation can lead to HOM-RO<sub>2</sub> with less than  
150 10 carbon atoms which may also continue the autoxidation chain. Therefore, the abundance of HOM with less than 10  
151 carbon atoms (HOM-Frag) indicates the importance of alkoxy steps. Secondly, with increasing functionalization, H-shifts  
152 retaining the carbon backbone become more likely (Vereecken et al., 2007) which will lead to a next generation of C<sub>10</sub>-  
153 HOM-RO<sub>2</sub>. Such alkoxy peroxy steps can continue the autoxidation chain (Mentel et al., 2015). Interestingly, by coupling of  
154 an alkoxy and a peroxy step, the parity of the number of oxygen atoms in the HOM-RO<sub>2</sub> changes, while in pure autoxidation  
155 steps the oxygen parity remains the same. Therefore, a parity change of the oxygen number can be used as an indication of  
156 alkoxy step abundance (Kang, 2021).

157 In summary we will use the changes in contribution and relative signal of the different families and classes to judge the  
158 impact of shifting from low to high HO<sub>2</sub>/RO<sub>2</sub> on the α-pinene photooxidation pathway.



## 159 1.2 Control of $\alpha$ -pinene OH turnover

160 One important concept of the conducted experiments is the constant OH availability to  $\alpha$ -pinene in the mixtures with CO to  
161 avoid effects of oxidant scavenging (McFiggans et al., 2019). Therefore, after each change in the HO<sub>2</sub>/RO<sub>2</sub> regime by CO  
162 addition, the OH level was readjusted to yield the same  $\alpha$ -pinene OH turnover and compensate for the OH consumed by CO.  
163 This OH adjustment ensures that the primary  $\alpha$ -pinene chemistry was kept the same and enables a direct comparison.

164 However, since experiments could only be performed at *about* the same OH levels, a normalization by the actual  $\alpha$ -pinene  
165 OH turnover is applied to the data. This compensates for the slight experimental imperfections and enables better  
166 comparison of experiment series with different boundary conditions. The turnover in steady state is given in **Eq. (1)**. Here  
167 the subscript “SS” denotes steady state condition for the concentrations of  $\alpha$ -pinene and OH,  $k_{OH}$  is the  $\alpha$ -pinene OH reaction  
168 rate constant.

$$turnover_{\alpha\text{-pinene}+OH} = k_{OH} * [\alpha\text{-pinene}]_{SS} * [OH]_{SS} \quad (1)$$

169 This normalization also directly shows the yield of certain oxidation product or product group per  $\alpha$ -pinene consumed by  
170 OH.

## 171 1.3 Derivation of effect on condensable mass from gas-phase measurement

172 A simple proxy for the condensable mass from HOM products can be calculated from the steady-state HOM-signals  
173 measured by the NO<sub>3</sub>-CIMS, assuming condensation for all low volatility HOM-compounds and no back evaporation into  
174 the gas phase. To only take low volatility products into account we used all detected formula compositions with  
175  $M > 230 \text{ g mol}^{-1}$  and weighted them with their molar mass. The reasoning behind this threshold can be found in **Sect. 4.4**. All  
176 contributions were summed up and normalized with the  $\alpha$ -pinene OH turnover for the comparison between the low and high  
177 HO<sub>2</sub>/RO<sub>2</sub> cases (**Eq. (2)**).

$$mass\ weighted\ signal\ sum = \frac{\sum_{i=0}^i S_i * M_i}{turnover_{\alpha\text{-pinene}+OH}} \quad (2)$$

178 We also estimated the expected SOA mass formed using the calibration factor obtained for sulfuric acid for our NO<sub>3</sub>-CIMS  
179 instrument in a calibration setup (see supplement **Sect. S1**). From this we calculated an upper boundary concentration of  
180 detected HOM-compounds in the gas phase under the assumption that sulfuric acid clusters with nitrate at the collision limit,  
181 yielding maximum sensitivity (a common approach, see for example Ehn et al. (2014), Pullinen et al. (2020)).

182 The calculated gas phase concentration was then used in the steady state equation describing the relationship between gas  
183 and particle phase concentrations of a single compound  $i$  shown in **Eq. (3)**.

$$m_{i,seed}(p) = \frac{m_{i,seed}(g) * k_{cond,i}}{k_{particleLoss} + k_{evap,i}} \quad (3)$$





184 **Equation (3)** shows that the steady state particle phase (mass) concentration  $m_{i,seed}(p)$  of compound  $i$  in presence of seed in  
185 the chamber is only dependent on the steady state gas phase concentration  $m_{i,seed}(g)$ , the condensation rate and evaporation  
186 rate constants  $k_{cond,i}$ ,  $k_{evap,i}$  of  $i$  (to and from the particles) and the particle loss rate constant  $k_{particleLoss}$  in the chamber.  
187 The condensation rate can be calculated (see supplement **Sect. S6**), and the particle loss rate constant was measured by  
188 observation of the particle loss in the chamber after ending the seed addition (details in the supplement **Sect. S2**). The  
189 evaporation rate was assumed to be negligible for the investigated HOM-compounds.  
190 For the SOA yield calculation, we calculate a corrected organic mass  $m_{SOA}$  from the organic mass  $m_{AMS}$  measured by aerosol  
191 mass spectrometry (AMS) and the fraction expected to be lost on the seed particles compared to the overall loss on particles  
192 and chamber wall as shown in **Eq. (4)** (McFiggans et al., 2019).

$$m_{SOA} = m_{AMS} * \frac{k_{cond} + k_{wall}}{k_{cond}} \quad (4)$$

193 In **Eq. (4)** we use the condensation rate constant  $k_{cond}$  calculated for one major HOM-product ( $C_{10}H_{16}O_7$ ) and the average  
194 HOM-Mon wall loss rate  $k_{wall}$  which was determined by switching off the UVC light and observing the decay of  
195 photooxidation products in the  $NO_3$ -CIMS. The wall loss determination, as well as SOA mass correction were described  
196 before in Sarrafzadeh et al. (2016) and McFiggans et al. (2019).

## 197 2 Experimental methods

### 198 2.1 Chamber setup

199 Experiments were conducted in the Jülich SAPHIR STAR chamber, which is the modern successor of the JPAC setup  
200 (Mentel et al., 2009). The basic concepts are the same as in JPAC, but each parameter is set, controlled, and monitored in a  
201 program. The chamber was operated as a continuously stirred tank reactor. It is a borosilicate glass cylinder ( $l=2.5$  m,  $d=1$  m)  
202 with a volume of 2000 L and all equipment inside the chamber is either glass or glass coated steel (SilcoTek GmbH).

203 With an inflow of  $32 \text{ L min}^{-1}$ , the residence time in the chamber was approximately 63 minutes with a fan ensuring mixing  
204 within minutes. In contrast to the JPAC chamber, the stirring is conducted perpendicular to the cylinder axis, as opposed to  
205 coaxial. Chamber inflow is split into two humidified clean air flows (mixed from  $N_2$  and  $O_2$ ) of about equal volume, one  
206 with added oxidant (here  $O_3$ ), the other with added VOC and other trace gases (here  $\alpha$ -pinene and CO). All experiments were  
207 performed at a relative humidity of 50 % and at  $20 \text{ }^\circ\text{C}$ . Temperature stability is ensured by the climate-controlled  
208 surrounding of the chamber.

209  $\alpha$ -Pinene ( $\geq 99$  % purity, Sigma-Aldrich Merck KGaA) was introduced via liquid injection with a syringe pump (Fusion  
210 4000, CHEMYX Inc.) into a heated glass bulb and flushed by a stream of  $1 \text{ L min}^{-1}$  into the chamber. CO was added from a





211 gas bottle (10% CO in N<sub>2</sub>, Messer SE & Co. KGaA). Ozone was directly produced photolytically before injection with a  
212 self-built ozone generator.

213 OH is produced in the chamber by ozone photolysis using two UV-C lamps with a wavelength of 254 nm and subsequent  
214 reaction of O(<sup>1</sup>D) with water vapor. The lamps are mounted in closed quartz cylinders in the middle of the chamber,  
215 vertically to the cylinder axis and light intensity can be varied with a movable shielding installed around the lamps. The  
216 shielding allows an exact percentage of the lamp to be covered, thus controlling the amount of OH produced in the chamber.

217 The OH radical concentration after CO addition was adjusted by setting the shielding of the UVC lamps and a slight  
218 adjustment of O<sub>3</sub> inflow. The applied J(O<sup>1</sup>D) values in different phases were calculated to be in the range of 0.8·10<sup>-3</sup> to  
219 2.4·10<sup>-3</sup> s<sup>-1</sup>.

220 In some of the experiments, ammonium sulfate (≥99 % purity, Merck KGaA) seed particles were added to the system to  
221 provide a surface for the condensation of organic material. The aerosol was produced with a modified TSI atomizer (Model  
222 3076, TSI GmbH) and dried to 50% relative humidity.

223 VOC concentrations in the chamber were measured using proton-transfer-reaction mass spectrometry (PTR-TOF-MS;  
224 Ionicon GmbH). CO<sub>2</sub>, CO, H<sub>2</sub>O (G2401 Cavity Ringdown Spectrometer, Picarro Inc.), NO, NO<sub>x</sub> (NCLD899, Eco Physics  
225 GmbH with a home-built photolytic converter) and O<sub>3</sub> (O342e, Envea GmbH) were additionally monitored. Particle  
226 distribution and concentration were measured with a condensation particle counter (CPC, Model 3788, TSI GmbH) and a  
227 scanning mobility particle sizer (SMPS; Model 3080, TSI GmbH) with a CPC (Model 3788, TSI GmbH). The aerosol  
228 composition was measured with a high-resolution aerosol mass spectrometer (HR-TOF AMS; Aerodyne Inc.).

229 In all experiments, VOC, O<sub>3</sub>, and SMPS+CPC sampling switched between inlet and outlet of the chamber to measure the  
230 input concentrations as well as the concentrations in the reactor. The flow control system of the chamber adapts to these  
231 switches so that the inflow into the chamber stays constant.

232 All results discussed here were observed under steady-state conditions when all parameters were constant. For each steady  
233 state, the OH concentration was calculated from the decay of α-pinene as described by Kiendler-Scharr et al. (2009).  
234 **Equation (5)** is derived from the mass balance of α-pinene at steady state. The steady state OH concentration [OH]<sub>SS</sub>  
235 depends on the amount of α-pinene consumed by reaction with OH and the reaction with O<sub>3</sub>, as well as the flush out.

$$[OH]_{SS} = \frac{F * \frac{[VOC]_{in} - [VOC]_{SS}}{[VOC]_{SS}} - k_{O_3} * [O_3]_{SS}}{k_{OH}} \quad (5)$$

236 Here, F is the total flow and V the volume of the chamber. The subscript “SS” indicates steady-state concentrations, while  
237 [VOC]<sub>in</sub> represents the α-pinene concentration entering the chamber. k<sub>o3</sub> and k<sub>OH</sub> represent the reaction rate constants of α-  
238 pinene with the corresponding oxidant. We applied rate coefficients of k<sub>o3</sub>=5.36·10<sup>-11</sup> cm<sup>3</sup>·s<sup>-1</sup> (Atkinson and Arey, 2003) and



239  $k_{OH}=9.25 \cdot 10^{-17} \text{ cm}^3 \cdot \text{s}^{-1}$  (Cox et al., 2020) at 20 °C. The uncertainty of the OH calculation was estimated as 20 % by Wildt et  
 240 al. (2014).

## 241 2.2 Experiment conditions

242 An overview of the experiments and their boundary conditions can be found in **Table 1**. Four experiments were performed  
 243 in total. In two of the experiments ammonium sulfate seeds were added leading to a total particle surface in the chamber on  
 244 the order of  $8 \cdot 10^{-4} \text{ m}^2 \text{ m}^{-3}$  and organic loadings of about  $3 \text{ ug m}^{-3}$  in the photooxidation stage. The *Exp2* experiment is a  
 245 consecutive combination of a seeded, followed by a non-seeded experiment to provide direct insight into the effect of seed  
 246 presence on the system.

247 As the OH radical is produced by photolysis of ozone and  $\alpha$ -pinene reacts with ozone, it is important to know the relative  
 248 contribution of the  $\alpha$ -pinene consumption by OH and by  $\text{O}_3$ . This is achieved by comparing the turnover of  $\alpha$ -pinene with  
 249 OH and  $\text{O}_3$  respectively. The results can be found in **Table 1**. The listed results are for the low  $\text{HO}_2/\text{RO}_2$  conditions, but  
 250 nearly identical values were reached after the  $\text{HO}_2/\text{RO}_2$  shift.

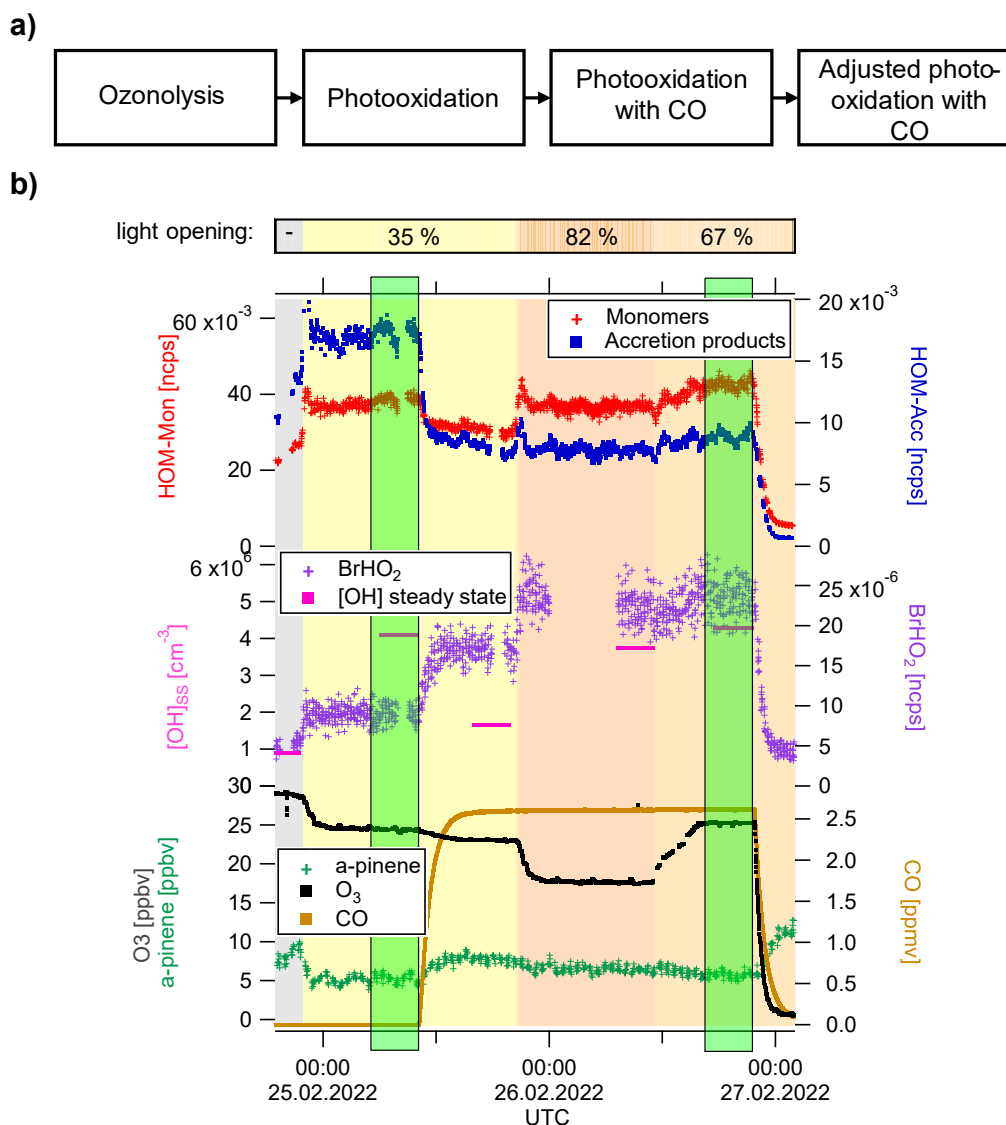
251 **Table 1. Overview of experimental conditions**

Name	Experiment description	[VOC] <sub>in</sub>	[CO] <sub>in</sub>	[OH] <sub>ss</sub> at low $\text{HO}_2/\text{RO}_2$	Contribution of OH to turnover at low $\text{HO}_2/\text{RO}_2$	Particle surface at low $\text{HO}_2/\text{RO}_2$	Organic mass concentration at low $\text{HO}_2/\text{RO}_2$
<i>Exp1</i>	<i>pure gas phase (1)</i>	10 ppbv	2.5 ppmv	$4.1\text{E}+6 \text{ cm}^{-3}$	80 %	-	-
<i>Exp2.1</i>	<i>seeded (1)</i>	10 ppbv	2.5 ppmv	$1.0\text{E}+7 \text{ cm}^{-3}$	91 %	$8.7\text{E}-4 \text{ m}^2 \text{ m}^{-3}$	$3.4 \text{ } \mu\text{g m}^{-3}$
<i>Exp2.2</i>	<i>unseeded (2)</i>	10 ppbv	2.5 ppmv	$1.3\text{E}+7 \text{ cm}^{-3}$	93 %	-	-
<i>Exp3</i>	<i>seeded (2)</i>	10 ppbv	2.5 ppmv	$1.4\text{E}+7 \text{ cm}^{-3}$	79 %	$6.8\text{E}-4 \text{ m}^2 \text{ m}^{-3}$	$2.7 \text{ } \mu\text{g m}^{-3}$

252



## 253 2.3 Experimental procedure



254

255 **Figure 2:** a) Experiment flow scheme b) Exemplary timeseries of *Exp1* experiment showing HOM-Mon and HOM-Acc  
256 product sum (top panel), calculated OH concentration and BrHO<sub>2</sub> signal (middle panel), and ozone,  $\alpha$ -pinene and CO  
257 concentrations (bottom panel). Background color represents light intensity. Highlighted in green are the low HO<sub>2</sub>/RO<sub>2</sub>  
258 steady state and the steady state at high HO<sub>2</sub>/RO<sub>2</sub> (addition of CO and adjusted oxidant level).

259 All experiments started with  $\alpha$ -pinene ozonolysis followed by illumination of the UVC-lights to induce the reaction with  
260 OH. A general flow scheme of the experiment can be found in **Fig. 2**, together with one exemplary timeseries of the  
261 unseeded experiment *Exp1*. After the photooxidation steady state, CO was added to the system. In the displayed *Exp1*  
262 experiment the OH concentration was adjusted in three steps to approach the desired value. First the UVC-light opening was  
263 adjusted and then O<sub>3</sub> was added, and the UVC-light opening was adjusted again. In some experiments initially the effect of



264 CO on the unchanged system was observed, before the adjustment of OH. In other experiments (*Exp2.2*, *Exp3*) the  
265 adjustment of the  $\alpha$ -pinene OH turnover via ozone concentration and UVC-light opening were made simultaneously with the  
266 CO addition. Highlighted in green are the steady states with the “same” OH concentration characterized by low and high  
267  $\text{HO}_2/\text{RO}_2$ , which were used for analysis and interpretation.

#### 268 **2.4 Model calculation for $\text{HO}_2/\text{RO}_2$ ratio estimation**

269 Box model calculations were performed applying the MCM v3.3.1 chemistry (Jenkin et al., 1997; Saunders et al., 2003)  
270 under the boundary conditions of the SAPHIR-STAR chamber. All calculations were performed with the institute software  
271 package EASY which uses FACSIMILE to solve the differential equations (EASY Version 5.69b). More details about the  
272 model parameters can be found in the supplement **Sect. S3**. The model calculations reproduced the primary observables  
273  $\alpha$ -pinene,  $\text{O}_3$ , CO, and OH within the experimental uncertainties. The box-model results were used to characterize the  
274  $\text{HO}_2/\text{RO}_2$  ratio of the chemical systems, as no direct measurement of these parameters was available. The observed cluster  
275 signal  $\text{BrHO}_2^-$  follows the modelled  $\text{HO}_2$  concentration (**Fig. 3**).

276 The model predicts a shift of the  $\text{HO}_2/\text{RO}_2$  ratio from about 0.01 to about 1 by CO addition and oxidant adjustment, an  
277 increase by two orders of magnitude. Owing to lack of observations to verify model results, we will consider only the  
278 magnitude of  $\text{HO}_2/\text{RO}_2$  here. The model results show that indeed a major shift from  $\text{RO}_2+\text{RO}_2$  to  $\text{RO}_2+\text{HO}_2$  reactions can be  
279 expected.

280 We further used the modelled  $\text{RO}_2$  and  $\text{HO}_2$  concentrations to estimate the relative importance of pathways for individual  
281 (observed) HOM- $\text{RO}_2$ . For that we applied two generic rate coefficients  $k_{\text{RO}_2\text{HO}_2}$  and  $k_{\text{RO}_2\text{RO}_2}$ . As the rate coefficient for the  
282  $\text{RO}_2+\text{HO}_2$  termination to a hydroperoxide  $k_{\text{RO}_2\text{HO}_2}$  we used the value specified in the MCM ( $1.85 \cdot 10^{-11} \text{ cm}^3 \cdot \text{s}^{-1}$  at  $20^\circ \text{C}$   
283 (Jenkin et al., 1997; Saunders et al., 2003)). We chose a  $k_{\text{RO}_2\text{RO}_2}$  of  $5 \cdot 10^{-12} \text{ cm}^3 \cdot \text{s}^{-1}$  as the approximated reaction rate of the  
284  $\text{RO}_2+\text{RO}_2$  reactions. This value applies to all possible reactions (accretion product, monomer, and alkoxy formation) and is  
285 in the range of  $k_{\text{RO}_2\text{RO}_2}$  utilized by Roldin et al. (2019) in the PRAM model.

#### 286 **2.5 Determination of oxidized VOCs, HOMs and $\text{HO}_2$**

287 Chemical ionization mass spectrometry (HR-TOF-CIMS) techniques were used to detect a range of gaseous compounds. For  
288 this, two atmospheric pressure interface time of flight mass spectrometers (APi-TOF-MS; Tofwerk AG) with different inlet  
289 systems were used simultaneously. General information about the APi-TOF-MS instrument can be found in Junninen et al.  
290 (2010).

291 A long TOF (LTOF) (Resolution  $\sim 8500$  for peaks at  $>200 \text{ m/Q}$ ) was coupled with the multi-scheme ionization inlet (MION;  
292 Karsa Oy). The setup of the inlet is described in detail by Rissanen et al. (2019). The distinctive feature of the MION inlet is  
293 the switching between two reagent ions. Here, nitrate was used to detect closed-shell HOMs, as well as HOM- $\text{RO}_2$ . Bianchi  
294 et al. (2019) suggested to define HOM as products stemming from autoxidation containing more than 6 oxygen. In our

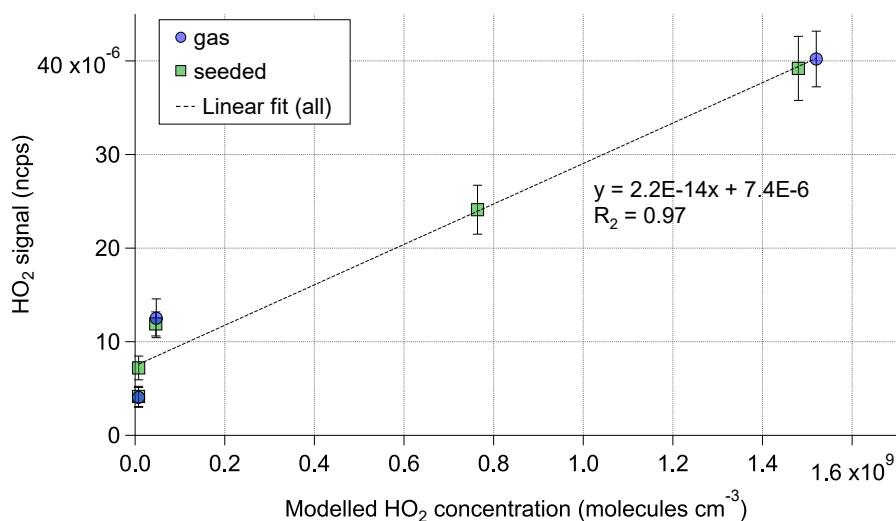


295 overall analysis we decided to also include fragments and monomers containing 5 or in a few cases 4 oxygens (see peaklist  
 296 in supplement **Sect. S4**) as we are interested to see if the importance of these less oxidized (but still with NO<sub>3</sub>-CIMS  
 297 detectable) products increases at higher HO<sub>2</sub>/RO<sub>2</sub>. However, in all considerations regarding SOA formation we furthermore  
 298 set a molar weight threshold which automatically excluded any products with less 6 oxygens.

299 As the second reagent ion, bromide was used to detect less oxidized products and the HO<sub>2</sub> radical (Albrecht et al., 2019;  
 300 Sanchez et al., 2016). The nitrate ion source had a reaction time of 600 ms, while the bromide ion source had a shorter  
 301 reaction time of 60 ms. For all experiments an inlet flow of 10 L min<sup>-1</sup> was used and the ionization scheme was switched  
 302 every 10 minutes.

303 In the data evaluation the first step was the separation of the timeseries of the two reagent ions. The data was subsequently  
 304 processed with Tofware (Version 3.2.3, Tofwerk AG) using the high resolution timeseries workflow. No transmission  
 305 correction was performed as previous measurements showed an approximately flat relative transmission curve in the mass  
 306 region of interest. The analyte signals were normalized with the reagent ion signal (NO<sub>3</sub><sup>-</sup> and HNO<sub>3</sub>NO<sub>3</sub><sup>-</sup> for nitrate and Br<sup>-</sup>  
 307 and BrH<sub>2</sub>O<sup>-</sup> for bromide).

308 Since no direct HO<sub>2</sub> calibration was available, the HO<sub>2</sub> signal in the Br-MION-CIMS was used to compare the levels of HO<sub>2</sub>  
 309 relative to each other in the different phases of the experiment. The comparison of the measured HO<sub>2</sub> signal to the modelled  
 310 HO<sub>2</sub> concentration shows a good linear relation between the model predictions and observations.



311  
 312 **Figure 3: Modelled HO<sub>2</sub> concentration vs. normalized HO<sub>2</sub> signal for each steady state of Exp2. HO<sub>2</sub> is measured as the BrHO<sub>2</sub>**  
 313 **cluster and is normalized with the sum of the reagent ion Br<sup>-</sup> and its water cluster. The dotted line shows the linear fit to all (gas**  
 314 **phase and seeded) measurement points.**

315 **Figure 3** illustrates this for the example of the Exp2 experiment. A background signal of around ~1·10<sup>-5</sup> is observed as soon  
 316 as VOC and ozone are present in the reactor. The background HO<sub>2</sub> signal was not observed when only O<sub>3</sub> or only VOC were



317 in the system. As shown by the MCM modelling results HO<sub>2</sub> production of this strength is not expected in the α-pinene  
318 ozonolysis phase but this background phenomenon was observed before (Albrecht et al., 2019) and is not fully understood.

319 For the HOM molecules measured by the NO<sub>3</sub>-MION-CIMS the relative changes between different experiment phases are  
320 compared. For all detected HOM products the same detection sensitivity is assumed. Hyttinen et al. (2018) showed in  
321 quantum chemical calculations that HOMs containing 6 or more oxygen atoms have comparable sensitivity with the nitrate  
322 reagent ion. At this degree of oxidation it can be expected that the HOMs already contain multiple hydroperoxyl and/or  
323 hydroxy functional groups (Bianchi et al., 2019) prior to the termination step, making it unlikely that the sensitivity is  
324 strongly influenced by the termination group. Thus, the signal strength reflects the correct ranking of the observations and  
325 relative comparisons do not require calibration. Pullinen et al. (2020) studied the mass balance between condensable HOMs  
326 and formed particle mass and were able to find closure within a factor of 2.

327 A second CI-API-TOF was used to measure less oxidized species. It was configured with a CI inlet based on the design of  
328 Eisele and Tanner (1993) coupled to an HTOF (Resolution ~2700 for peaks at >200 m/Q) (ToFwerk AG) and was operated  
329 in positive mode with propylamine (C<sub>3</sub>H<sub>7</sub>NH<sub>2</sub>, Sigma-Aldrich, purity ≥99%) to detect the early generation RO<sub>2</sub> and  
330 oxidation products (Berndt et al., 2018). The propylamine was purified and added as an amine-N<sub>2</sub> mixture (flow:  
331 0.12 mL min<sup>-1</sup>) to the 30 L min<sup>-1</sup> sheath flow. Furthermore, the sheath flow air is humidified to optimize ionization. The  
332 instrument sampled 0.1 L min<sup>-1</sup> from the chamber, which was diluted with 9.9 L min<sup>-1</sup> for a sample flow of 10 L min<sup>-1</sup>. The  
333 dilution was necessary to reduce depletion of the primary ion (Hantschke, 2022).

### 334 **3 Results and Discussion**

335 In order to understand the effect of HO<sub>2</sub>/RO<sub>2</sub> on the gas phase product composition, we will present and compare two cases:  
336 The steady state without CO (low HO<sub>2</sub>/RO<sub>2</sub>) and the steady state with CO addition and OH adjustment by J(O<sup>1</sup>D) and O<sub>3</sub>  
337 (high HO<sub>2</sub>/RO<sub>2</sub>). The modelling results predicted HO<sub>2</sub>/RO<sub>2</sub> of about 1/100 and of about 1/1 for these two cases respectively.  
338 The modelling results show that the HO<sub>2</sub>/RO<sub>2</sub> ratio changes by two orders of magnitude, because [RO<sub>2</sub>] was reduced by  
339 about a factor of three, while [HO<sub>2</sub>] was increased by a factor of 30. Consequently, HO<sub>2</sub> reactions were almost negligible at  
340 low HO<sub>2</sub>/RO<sub>2</sub> while RO<sub>2</sub>+RO<sub>2</sub> reactions can still contribute at high HO<sub>2</sub>/RO<sub>2</sub>.

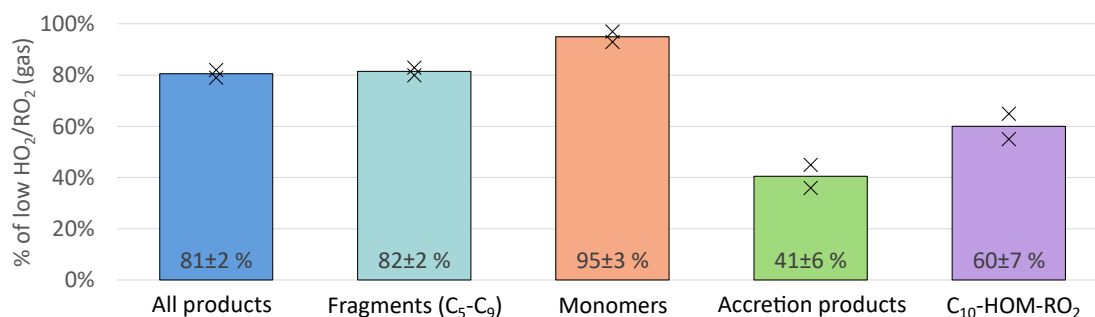
341 Assuming correctly modelled [HO<sub>2</sub>] and [RO<sub>2</sub>], we calculated the competition between HO<sub>2</sub> and RO<sub>2</sub> reactions for each  
342 (observed) RO<sub>2</sub> expressed in form of pseudo first order rate coefficients in  $k_{RO_2HO_2} \cdot [HO_2]$  or  $k_{RO_2RO_2} \cdot [RO_2]$ . Herein  
343 [RO<sub>2</sub>] is the sum of all RO<sub>2</sub> species as defined in the MCM v3.3.1. For all experiments the results of our calculations indicate  
344 that the sink for HOM-RO<sub>2</sub> is dominated by RO<sub>2</sub>+RO<sub>2</sub> reactions at low HO<sub>2</sub>/RO<sub>2</sub> (~98 % contribution), while at high  
345 HO<sub>2</sub>/RO<sub>2</sub> RO<sub>2</sub>+HO<sub>2</sub> contributed ~75 %. As the rate coefficients are not well known and we cannot verify the modelling  
346 results for HO<sub>2</sub> and RO<sub>2</sub> our calculations serve solely as an indication of expected trends in the chemical system.



### 347 3.1 Impact on overall HOM-formation

348 The top panel of **Fig. 2** shows the timeseries of HOM-Mon and HOM-Acc products. The HOM-Mon signal recovers after  
349 the oxidant adjustment, while the HOM-Acc signal is significantly suppressed at high  $\text{HO}_2/\text{RO}_2$ . This indicates that the shift  
350 from low to high  $\text{HO}_2/\text{RO}_2$  substantially impacts the termination reactions, shifting formation from the HOM-Acc product  
351 channel ( $\text{RO}_2+\text{RO}_2$ ) to the HOM-Mon channel.

352 An overview of the results for the product classes defined in the method section is shown in **Fig. 4**. Plotted are the average  
353 ratios of signal in the  $\text{NO}_3$ -CIMS in the high  $\text{HO}_2/\text{RO}_2$  steady state compared to the low  $\text{HO}_2/\text{RO}_2$  steady state. For better  
354 comparison, all experiment phases were normalized to the actual  $\alpha$ -pinene OH turnover. The overall HOM-signal was lower  
355 at high  $\text{HO}_2/\text{RO}_2$  showing a reduction of about 20 %. Most distinctive, the HOM-Acc were strongly reduced by about 60 %.  
356 A reduction of HOM-Acc by addition of CO was observed before by McFiggans et al. (2019), however there the OH  
357 concentration was not kept constant. The HOM-Frag ( $5 \leq C < 10$ ) also show a reduction of about 20 %. At high  $\text{HO}_2/\text{RO}_2$   
358  $\text{C}_{10}$ -HOM- $\text{RO}_2$  were also reduced significantly by about 40 %.

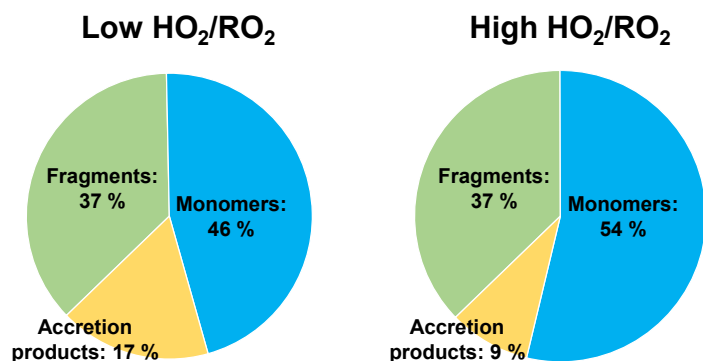


359

360 **Figure 4: Overview of average, relative change in product classes detected in  $\text{NO}_3$ -CIMS between low and high  $\text{HO}_2/\text{RO}_2$  case**  
361 **(both normalized to  $\alpha$ -pinene OH turnover) for pure gas phase experiments. Bars represent average of the two experiments,**  
362 **markers represent individual experiments.**

363 The HOM-Mon signal level remained about the same at low and high  $\text{HO}_2/\text{RO}_2$ . Without reduction in the HOM- $\text{RO}_2$   
364 precursors a reduction of HOM-Acc should lead to an increase in HOM-Mon, as each HOM-Acc is formed from one  
365 HOM- $\text{RO}_2$  (HOM- $\text{RO}_2+\text{RO}_2$ ) or potentially even two HOM- $\text{RO}_2$  (HOM- $\text{RO}_2+\text{HOM-RO}_2$ ). Of course, the presence of  $\text{HO}_2$   
366 could reduce the alkoxy formation, and thus fragmentation of HOM- $\text{RO}_2$ . This missing sink could lead to an additional  
367 HOM-Mon source compared to the low  $\text{HO}_2/\text{RO}_2$  case. However, the distribution of the product classes at low and high  
368  $\text{HO}_2/\text{RO}_2$  (**Fig. 5**) shows that contributions are shifted from HOM-Acc to HOM-Mon, while the contribution of HOM-Frag  
369 remains constant.

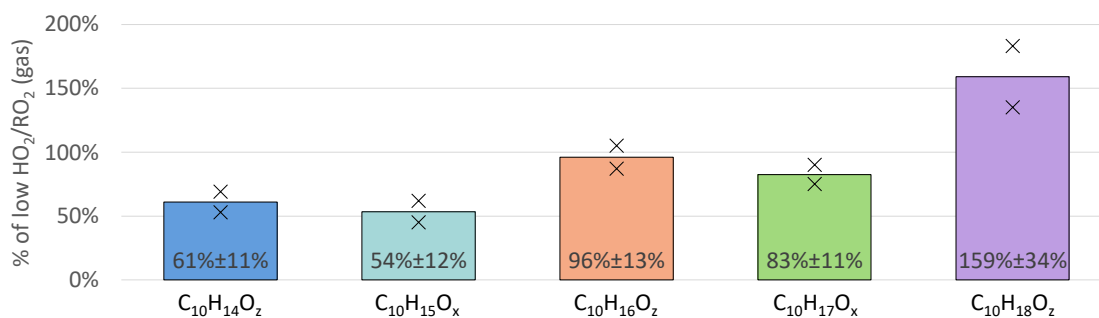




370

371 **Figure 5: Average contribution of the closed shell product classes to overall HOM-product signal in the low and high  $\text{HO}_2/\text{RO}_2$**   
372 **cases (pure gas phase experiments).**

373 Further changes in the product distribution become evident when considering the individual HOM-Mon families as shown in  
374 **Fig. 6.** The  $\text{C}_{10}\text{H}_{15}\text{O}_x$  peroxy radical family and the related  $\text{C}_{10}\text{H}_{14}\text{O}_z$  family (carbonyl compounds) show the strongest  
375 suppression with a decrease of about 40 % at high  $\text{HO}_2/\text{RO}_2$ . For the  $\text{C}_{10}\text{H}_{17}\text{O}_x$  peroxy radical family the suppression was  
376 less pronounced with a 17 % reduction. In contrast, the  $\text{C}_{10}\text{H}_{16}\text{O}_z$  family remained about the same while the  $\text{C}_{10}\text{H}_{18}\text{O}_z$  family  
377 showed a strong increase at high  $\text{HO}_2/\text{RO}_2$ .



378

379 **Figure 6: Overview of average, relative change in monomer families detected in  $\text{NO}_3$ -CIMS between low and high  $\text{HO}_2/\text{RO}_2$  case**  
380 **(both normalized to  $\alpha$ -pinene OH turnover) for pure gas phase experiments. Bars represent average of the two experiments,**  
381 **markers represent individual experiments.**

382 The suppression of  $\text{C}_{10}$ -HOM- $\text{RO}_2$  of only about 40 % compared to the reduction of overall  $[\text{RO}_2]$  by ~70 % in the model  
383 calculations shows that in many instances the autoxidation is too efficient to be out-competed by the  $\text{RO}_2+\text{HO}_2$  termination  
384 reaction, which is several times faster than  $\text{RO}_2+\text{RO}_2$  reactions.

385 Furthermore, the signal weighted O/C ratio of the monomer class does not change between low and high  $\text{HO}_2/\text{RO}_2$  ( $0.70 \pm$   
386  $0.01$ ). If the  $\text{HO}_2$  termination would interrupt the autoxidation chain, a lower oxidation level would be expected at high  
387  $\text{HO}_2/\text{RO}_2$ . The unchanged oxidation level and the suppression of HOM-Acc, indicate that the average autoxidation rate must  
388 be faster than  $k_{\text{RO}_2\text{HO}_2} \cdot [\text{HO}_2]$ , while the average accretion rate for  $k_{\text{HOM-RO}_2+\text{RO}_2} \cdot [\text{RO}_2]$  must be slower. In conclusion, the  
389 change in  $\text{HO}_2/\text{RO}_2$  should essentially impact the distribution of the HOM- $\text{RO}_2$  termination products.



### 390 3.2 Impact on HOM-RO<sub>2</sub>

391 C<sub>10</sub>-HOM-RO<sub>2</sub> are key to understand the changes in the HOM product distribution. Therefore, we will first discuss the  
392 changes in the HOM-RO<sub>2</sub> and then the changes in the closed shell products.

393 The C<sub>10</sub> peroxy radical class consists of the C<sub>10</sub>H<sub>15</sub>O<sub>x</sub> and C<sub>10</sub>H<sub>17</sub>O<sub>x</sub> families which were reduced to 54 % and 83 %,  
394 respectively when comparing the high and low HO<sub>2</sub>/RO<sub>2</sub> cases (**Fig. 6**, light blue and green bars). The observed reduction in  
395 C<sub>10</sub>-HOM-RO<sub>2</sub> is significantly smaller than the overall RO<sub>2</sub> concentration reduction predicted by the MCM model results  
396 (reduction to ~30 %). In the following paragraphs, we present a plausibility consideration to assess if these observed changes  
397 are consistent with our expectations from modelling results and reaction rates.

398 The change in the steady state concentration of a compound is always defined by the changes in its sources and sinks. The  
399 source of a HOM-RO<sub>2</sub> is the intramolecular reaction of a precursor RO<sub>2</sub> and thus the HOM-RO<sub>2</sub>'s source is reduced if the  
400 steady state concentration of the precursor RO<sub>2</sub> is reduced. However, assuming the source term of the precursor RO<sub>2</sub> is the  
401 same in low and high HO<sub>2</sub>/RO<sub>2</sub> (due to the constant  $\alpha$ -pinene OH turnover) and the precursor RO<sub>2</sub>'s sink term is dominated  
402 by the fast autoxidation in both cases, then the RO<sub>2</sub>'s steady state concentration would not be significantly changed. This  
403 consideration is only applicable for RO<sub>2</sub> where autoxidation dominates the sink term at low and high HO<sub>2</sub>/RO<sub>2</sub>. However,  
404 the unchanged oxidation level of the HOM-Mon indicates that once the autoxidation is initiated it out-competes the possible  
405 termination reactions.

406 In this case, the change in steady state concentration of the HOM-RO<sub>2</sub> will be defined by the changes in the sink terms.  
407 Owing to the faster reaction of RO<sub>2</sub>+HO<sub>2</sub> compared to RO<sub>2</sub>+RO<sub>2</sub> the chemical sink for all RO<sub>2</sub> including HOM-RO<sub>2</sub> with  
408 slower autoxidation rates increased, which leads to a reduction in the steady state concentration of RO<sub>2</sub> in general, despite  
409 holding the primary RO<sub>2</sub> source term constant.

410 For steady state conditions, we can estimate the expected effect of high and low HO<sub>2</sub>/RO<sub>2</sub> on the RO<sub>2</sub> ratio for those HOM-  
411 RO<sub>2</sub> with production directly linked to the primary production ( $k_{OH}[OH]\cdot[\alpha\text{-pinene}]$ ) with negligible further autoxidation.  
412 The necessary equations and assumptions can be found in supplement **Sect. S5**. We assume the same primary production at  
413 low and high HO<sub>2</sub>/RO<sub>2</sub> and that the reaction with HO<sub>2</sub>, the reaction with RO<sub>2</sub> and the wall loss are the only significant loss  
414 pathways. At high HO<sub>2</sub>/RO<sub>2</sub>, a reduction to 80 % is expected if the rate coefficient  $k_{RO_2HO_2}$  ( $1.85\cdot 10^{-11}$  cm<sup>3</sup>·s<sup>-1</sup> at 20 °C  
415 (Jenkin et al., 1997; Saunders et al., 2003)) is 5 times faster than  $k_{RO_2RO_2}$  (leading to  $k_{RO_2HO_2}=3.7\cdot 10^{-12}$  cm<sup>3</sup>·s<sup>-1</sup>). A reduction  
416 to 60 % is expected if  $k_{RO_2HO_2}$  is 8 times faster than  $k_{RO_2RO_2}$ . These reductions are in the range of what is observed for the  
417 C<sub>10</sub>-HOM-RO<sub>2</sub>. Of course, the approach of using generalized bulk rate constants is limited, but the resulting values for  
418  $k_{RO_2RO_2}$  were clearly within the range of rate coefficients expected for HOM-RO<sub>2</sub>+RO<sub>2</sub> reactions (Roldin et al., 2019)  
419 showing that the increased chemical sink is a plausible explanation for our observations.

420 The C<sub>10</sub>H<sub>15</sub>O<sub>x</sub> family is on average reduced by around 30 % more than the C<sub>10</sub>H<sub>17</sub>O<sub>x</sub> family (see **Fig. 6**). C<sub>10</sub>H<sub>15</sub>O<sub>x</sub> peroxy  
421 radicals are either formed by sequential oxidation of  $\alpha$ -pinene, e.g. from oxidation products like pinonaldehyde, or directly



422 from  $\alpha$ -pinene via the H-abstraction pathway (Shen et al., 2022). Formation of pinonaldehyde and, even more so HOM  
423 formation via the H-abstraction channel, involve alkoxy steps. However, alkoxy radicals should be reduced at high  $\text{HO}_2/\text{RO}_2$   
424 since they are mainly formed by  $\text{RO}_2+\text{RO}_2$  reactions in the absence of  $\text{NO}_x$ . Thus, missing source terms add to the increased  
425 chemical sink by  $\text{HO}_2$  for  $\text{C}_{10}\text{H}_{15}\text{O}_x$  peroxy radicals.

426 Amine CIMS measurements enabled detection of the formula composition  $\text{C}_{10}\text{H}_{16}\text{O}_2$  (e.g. pinonaldehyde).  $\text{C}_{10}\text{H}_{16}\text{O}_2$  was  
427 reduced on average to  $71\% \pm 1\%$  at high  $\text{HO}_2/\text{RO}_2$  compared to low  $\text{HO}_2/\text{RO}_2$ . This supports that a fraction of the  $\text{C}_{10}\text{H}_{15}\text{O}_x$   
428 radical decrease at high  $\text{HO}_2/\text{RO}_2$  arose from suppression of  $\text{C}_{10}\text{H}_{16}\text{O}_2$  first generation products. In addition, a further  
429 suppression of HOM formation via the H-abstraction channel is likely. It should be noted that the reduction of  $\text{C}_{10}\text{H}_{16}\text{O}_2$  is  
430 smaller than that expected by the MCM model results. This might indicate that  $\text{HO}_2$  can also enable alkoxy radical steps to a  
431 certain degree as summarized by Jenkin et al. (2019) and postulated by e.g. Eddingsaas et al. (2012) as a source of  
432 pinonaldehyde in  $\text{HO}_2$  dominated systems.

433 According to the model calculations the pseudo first order rate coefficient  $k_{\text{RO}_2\text{HO}_2}[\text{HO}_2]$  is expected to be about  $0.03 \text{ s}^{-1}$  for  
434 the  $\text{RO}_2+\text{HO}_2$  reaction at high  $\text{HO}_2/\text{RO}_2$ . Consequently, only such HOM- $\text{RO}_2$  with autoxidation rates of  $\leq 0.03 \text{ s}^{-1}$  will be  
435 significantly lost by reaction with  $\text{HO}_2$  at the higher  $\text{HO}_2$  concentrations. However, typical isomerization rates of peroxy  
436 radicals in autoxidation are of the order of  $0.1 \text{ s}^{-1}$  and many are faster (Piletic and Kleindienst, 2022; Berndt, 2021).  
437 Therefore, reduction in a HOM- $\text{RO}_2$  is only expected when the faster termination rate of  $k_{\text{RO}_2\text{HO}_2}[\text{HO}_2]$  can compete with the  
438 autoxidation rate, i. e. when the autoxidation slows as the degree of oxidation increases on the specific HOM- $\text{RO}_2$ .

439 The increase in chemical sink strength by going from  $\text{RO}_2$  termination to  $\text{HO}_2$  termination is the main expected reason for  
440 the decrease in  $\text{C}_{10}\text{H}_{17}\text{O}_x$ . As discussed, the  $\text{C}_{10}\text{H}_{15}\text{O}_x$  family is subject to an additional decrease in the precursors due to the  
441 alkoxy steps necessary in the formation pathway. Since  $\text{C}_{10}\text{H}_{15}\text{O}_x$  were the main contributors to the  $\text{C}_{10}$ -HOM- $\text{RO}_2$  class  
442 their stronger reduction is reflected in the overall reduction of  $\text{C}_{10}$ -HOM- $\text{RO}_2$ .

### 443 3.2.1 Contribution of $\text{C}_{10}\text{H}_{15}\text{O}_x$ and $\text{C}_{10}\text{H}_{17}\text{O}_x$ families to HOM- $\text{RO}_2$

444 In the pure gas phase experiments, the contribution of the  $\text{C}_{10}\text{H}_{17}\text{O}_x$  family to the  $\text{C}_{10}$ -HOM- $\text{RO}_2$  class is  $23\% \pm 2\%$  on  
445 average in the low  $\text{HO}_2/\text{RO}_2$  case. In the high  $\text{HO}_2/\text{RO}_2$  case the contribution increases to  $31\% \pm 4\%$  on average. As  
446 discussed above the suggested pathways to  $\text{C}_{10}\text{H}_{15}\text{O}_x$  HOM- $\text{RO}_2$  may be additionally suppressed due to a decrease of alkoxy  
447 steps at high  $\text{HO}_2/\text{RO}_2$  reducing the entry channel into  $\text{C}_{10}\text{H}_{15}\text{O}_x$  HOM- $\text{RO}_2$ .

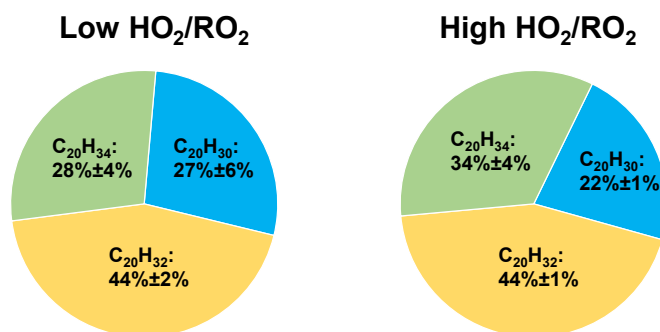
448 Nevertheless, the contribution of  $\text{C}_{10}\text{H}_{15}\text{O}_x$  is substantial in both experiment stages. Kang (2021) and Shen et al. (2022)  
449 reported that, in the photooxidation of  $\alpha$ -pinene, the HOM- $\text{RO}_2$  detected by  $\text{NO}_3$ -CIMS are dominated by the  $\text{C}_{10}\text{H}_{15}\text{O}_x$   
450 family, while  $\text{C}_{10}\text{H}_{17}\text{O}_x$  formation is the main expected OH reaction pathway described in literature (Berndt, 2021; Berndt et  
451 al., 2016; Xu et al., 2019).



452 This hints towards an effective pathway to HOM via  $C_{10}H_{15}O_x$ . A reason may be the fast opening of both carbon-rings in the  
453 bicyclic  $\alpha$ -pinene (Shen et al., 2022), or a four-ring opening in pinonaldehyde or similar compounds, for easy autoxidation.  
454 From our observations increasing the  $HO_2/RO_2$  ratio does increase the relative importance of the  $C_{10}H_{17}O_x$  family, but the  
455 change is less than 10 % in contribution.

456 Contribution of the two peroxy radical families to the HOM formation is also reflected in the composition of  $C_{20}$  HOM-Acc.  
457 **Figure 7** shows the average contributions of the  $C_{20}H_{30}O_z$ ,  $C_{20}H_{32}O_z$ , and  $C_{20}H_{34}O_z$  families in the low and high  $HO_2/RO_2$   
458 cases. Although the absolute amount of HOM-Acc was suppressed by 60 % the family distribution was similar,  $C_{20}H_{32}O_z$   
459 dominated, while  $C_{20}H_{30}O_z$  was lowest.  $C_{20}H_{30}O_z$  is formed from two members of the  $C_{10}H_{15}O_x$  family, while  $C_{20}H_{34}O_z$  is  
460 formed by two members of the  $C_{10}H_{17}O_x$  family.  $C_{20}H_{32}O_z$  is then a combination of a  $C_{10}H_{15}O_x-RO_2$  and  $C_{10}H_{17}O_x-RO_2$ .

461 Families that require one or two  $C_{10}H_{17}O_x$  peroxy radicals for their formation have a higher contribution than the  $C_{10}H_{17}O_x$   
462 family's contribution to  $C_{10}$ -HOM- $RO_2$ . Here, it is important to note that not only HOM- $RO_2$  can participate in HOM-Acc  
463 formation, but also traditional, less oxidized  $RO_2$  radicals (Berndt et al., 2018; Pullinen et al., 2020; McFiggans et al., 2019),  
464 which are not detectable by  $NO_3^-$ -CIMS. However, more oxidized peroxy radicals exhibit faster accretion rates (Berndt et al.,  
465 2018).



466

467 **Figure 7: Average contribution of the  $C_{20}H_{30}O_z$ ,  $C_{20}H_{32}O_z$ , and  $C_{20}H_{34}O_z$  family to the  $C_{20}$  HOM-Acc group signal in the low and**  
468 **high  $HO_2/RO_2$  cases (pure gas phase experiments). Not pictured is  $C_{20}H_{28}O_z$  due to its negligible signal (contribution ~1 %).**

469 The large contributions of  $C_{20}H_{32}O_z$  and  $C_{20}H_{34}O_z$  thus clearly show the general importance of the  $C_{10}H_{17}O_x$  peroxy radicals.  
470 The largest fraction, the  $C_{20}H_{32}O_z$  family reflects the importance of HOM- $C_{10}H_{15}O_x$  and the high abundance of lower  
471 oxidized  $C_{10}H_{17}O_x$  peroxy radicals. The fraction of  $C_{20}H_{34}O_z$  is smaller because their formation requires HOM- $C_{10}H_{17}O_x$   
472 radicals which are less abundant compared to HOM- $C_{10}H_{15}O_x$ , while the small fraction of  $C_{20}H_{30}O_z$  indicates that, despite the  
473 importance of HOM- $C_{10}H_{15}O_x$ , lower oxidized  $C_{10}H_{15}O_x$  are less important.

474 These results indicate the importance of mixed HOM-Acc formation by cross reactions of HOM- $RO_2$  and a lower oxidized  
475  $RO_2$ . The importance of mixed HOM-Acc is supported by the relatively small fractions of HOM-Acc products with very  
476 high oxygen numbers, which more likely stem from HOM- $RO_2$ +HOM- $RO_2$ . For example,  $C_{20}$ -HOM-Acc with 12 or more



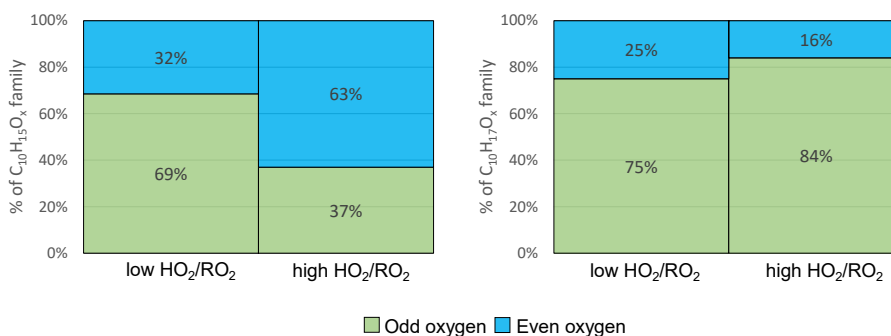
477 oxygen atoms contribute only around 30 % (low  $\text{HO}_2/\text{RO}_2$ : 26 %  $\pm$ 4 %, high  $\text{HO}_2/\text{RO}_2$ : 31 %  $\pm$ 2 %) of the signal in the  
478 product group.

479 Although the effect of the changed  $\text{HO}_2/\text{RO}_2$  ratio is small, a tendency to higher  $\text{C}_{20}\text{H}_{34}\text{O}_z$  contribution was observed. This is  
480 consistent with the observation of a slightly higher  $\text{C}_{10}\text{H}_{17}\text{O}_x$  contribution to the  $\text{C}_{10}$ -HOM  $\text{RO}_2$ . The stronger suppression of  
481 the  $\text{C}_{10}\text{H}_{15}\text{O}_x$  family at high  $\text{HO}_2/\text{RO}_2$  is the first indication for, and can be explained by, a reduction in the alkoxy radical  
482 formation.

### 483 3.2.2 Impact on HOM-Alkoxy radical formation

484 Alkoxy radicals (RO) are the second important radical type in the oxidation chain of  $\alpha$ -pinene. RO cannot be detected  
485 directly as they are highly unstable and thus have very low concentrations. However, as explained in Sect. Fehler! V  
486 erweisquelle konnte nicht gefunden werden. the parity change in the HOM- $\text{RO}_2$  families can be used as a diagnosis tool for  
487 the abundance of alkoxy steps (Kang, 2021). A second indicator for alkoxy steps is the abundance of HOM products with  
488 less than 10 C-atoms.

489 **Figure 8** shows the average contribution of  $\text{C}_{10}\text{H}_{15}\text{O}_x$  and  $\text{C}_{10}\text{H}_{17}\text{O}_x$  with an even and odd number of oxygens at low and  
490 high  $\text{HO}_2/\text{RO}_2$ .  $\text{C}_{10}\text{H}_{15}\text{O}_x$  radicals with an even number of oxygens contribute on average 32 % at low  $\text{HO}_2/\text{RO}_2$ . For  
491  $\text{C}_{10}\text{H}_{15}\text{O}_x$ , the autoxidation chain is expected to start from an even number of oxygen either from  $\text{C}_{10}\text{H}_{15}\text{O}_4$  (pinonaldehyde-  
492 like) (MCM v3.3.1 (Jenkin et al., 1997; Saunders et al., 2003) or from  $\text{C}_{10}\text{H}_{15}\text{O}_2$  ( $\text{C}_{10}\text{H}_{16}$  H-abstraction) (Berndt, 2021; Shen  
493 et al., 2022). Therefore, without the involvement of an alkoxy step, the parity of the oxygen number in the observed  
494  $\text{C}_{10}\text{H}_{15}\text{O}_x$  HOM- $\text{RO}_2$  is expected to be even. Due to the average contribution of  $\text{C}_{10}\text{H}_{15}\text{O}_{\text{odd}}$  of 69 % we conclude that at least  
495 one alkoxy step (or any odd number of alkoxy steps) must have taken place in most of the cases at low  $\text{HO}_2/\text{RO}_2$ .



496

497 **Figure 8: Average contribution of  $\text{O}_{\text{odd}}$  and  $\text{O}_{\text{even}}$  to the HOM- $\text{RO}_2$  families  $\text{C}_{10}\text{H}_{15}\text{O}_x$  (left) and  $\text{C}_{10}\text{H}_{17}\text{O}_x$  (right) signal in the low  
498 and high  $\text{HO}_2/\text{RO}_2$  cases (pure gas phase experiments).**

499 At high  $\text{HO}_2/\text{RO}_2$   $\text{C}_{10}\text{H}_{15}\text{O}_{\text{even}}$  contributed 63 % and the  $\text{C}_{10}\text{H}_{15}\text{O}_{\text{odd}}$  contribution was reduced to 37 %. This demonstrates a  
500 change in the number of alkoxy steps along the formation pathway of the observed HOM- $\text{RO}_2$  radicals. The increased  
501 contribution of  $\text{C}_{10}\text{H}_{15}\text{O}_{\text{even}}$  at high  $\text{HO}_2/\text{RO}_2$  lets us infer an even number of alkoxy steps as more common (0,2,4...). In the

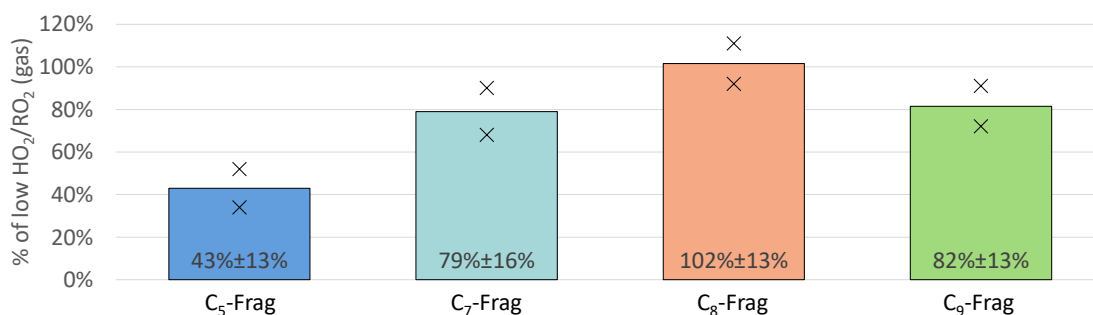


502 simplest case 1 or 2 alkoxy step take place at low  $\text{HO}_2/\text{RO}_2$  due to HOM-RO formation from  $\text{HOM-RO}_2+\text{RO}_2$  reactions,  
 503 while no or 1 alkoxy step take place at high  $\text{HO}_2/\text{RO}_2$ , because  $\text{HOM-RO}_2+\text{HO}_2$  produces none or less HOM-RO than  
 504  $\text{HOM-RO}_2+\text{RO}_2$ .

505 For  $\text{C}_{10}\text{H}_{17}\text{O}_x$  the entry channel into autoxidation is  $\text{C}_{10}\text{H}_{17}\text{O}_3$  with an odd number of oxygen atoms. Therefore, in  
 506 autoxidation without alkoxy steps the oxygen parity is expected to be odd. At low  $\text{HO}_2/\text{RO}_2$   $\text{C}_{10}\text{H}_{17}\text{O}_{\text{odd}}$  species contribute  
 507 75 % to the total  $\text{C}_{10}\text{H}_{17}\text{O}_x$  signal indicating that either none or an even number (2,4,...) of alkoxy steps occurred. At high  
 508  $\text{HO}_2/\text{RO}_2$  the odd contribution increases to 84 % (see **Fig. 8**). This result could indicate a low occurrence of alkoxy steps  
 509 even at low  $\text{HO}_2/\text{RO}_2$ , with a further decrease of alkoxy formation at high  $\text{HO}_2/\text{RO}_2$ . However, the observed shift is minor.

510 In any case the different responses of the  $\text{C}_{10}\text{H}_{15}\text{O}_x$  and  $\text{C}_{10}\text{H}_{17}\text{O}_x$  families to the reduction of HOM-RO<sub>2</sub> formation from  
 511  $\text{HOM-RO}_2+\text{RO}_2$  at high  $\text{HO}_2/\text{RO}_2$  indicate that there could be fundamental differences in the autoxidation chains of  
 512  $\text{C}_{10}\text{H}_{15}\text{O}_x$  and  $\text{C}_{10}\text{H}_{17}\text{O}_x$  (or the limit of the parity analysis). The parity analysis indicates a decrease in alkoxy steps at high  
 513  $\text{HO}_2/\text{RO}_2$ , but it cannot be directly inferred with certainty. However, decrease in alkoxy steps at high  $\text{HO}_2/\text{RO}_2$  is supported  
 514 by the observation of changes in HOM-Frag products.

515 On average the sum of all HOM-Frag products (detected compounds with  $5 \leq \text{C} < 10$  by  $\text{NO}_3^-$ -CIMS) showed a reduction of  
 516 around 20 % (pure gas phase experiments, see **Fig. 4**). Further trends become recognizable when separating the species  
 517 according to their carbon number. **Figure 9** shows the  $\text{C}_5$ ,  $\text{C}_7$ ,  $\text{C}_8$ , and  $\text{C}_9$  HOM-Frag at high  $\text{HO}_2/\text{RO}_2$  compared to the low  
 518  $\text{HO}_2/\text{RO}_2$  case, normalized to the  $\alpha$ -pinene OH turnover. The fragment group with  $\text{C}_6$  compounds is not included, as it  
 519 contributed less than 5 % of the fragment signal and contained few detected compounds.



520

521 **Figure 9: Overview of average, relative change in  $\text{C}_5$ ,  $\text{C}_7$ ,  $\text{C}_8$ ,  $\text{C}_9$  fragment groups detected in  $\text{NO}_3$ -CIMS between high and low**  
 522  **$\text{HO}_2/\text{RO}_2$  case (both normalized to  $\alpha$ -pinene OH turnover) for pure gas phase experiments. Bars represent average of the two**  
 523 **experiments, markers represent individual experiments.**

524 **Figure 9** shows a significant reduction in HOM-Frag with shorter carbon chain length:  $\text{C}_5$  HOM-Frag are reduced by around  
 525 60 % compared to the low  $\text{HO}_2/\text{RO}_2$  case. If we assume that the fragmentation of  $\text{C}_{10}$  compounds happens in consecutive  
 526 steps via scission of HOM-RO radicals (analogously to the MCM), this observation is in accord with decreasing importance  
 527 of alkoxy radical formation at high  $\text{HO}_2/\text{RO}_2$ .



528 Overall, all observations indicate strong involvement of RO in HOM formation as well as a reduced, but still significant,  
529 involvement of RO at high  $\text{HO}_2/\text{RO}_2$ , when  $\text{HO}_2$  chemistry dominates: This is supported by the change of the oxygen parity  
530 in  $\text{C}_{10}$ -HOM- $\text{RO}_2$ , and the decrease of fragmentation products, especially with lower carbon number, as well as the only  
531 moderate reduction in the observed  $\text{C}_{10}\text{H}_{16}\text{O}_2$  product (pinonaldehyde) and the still substantial importance of the  $\text{C}_{10}\text{H}_{15}\text{O}_x$   
532 HOM- $\text{RO}_2$  family at high  $\text{HO}_2/\text{RO}_2$ .

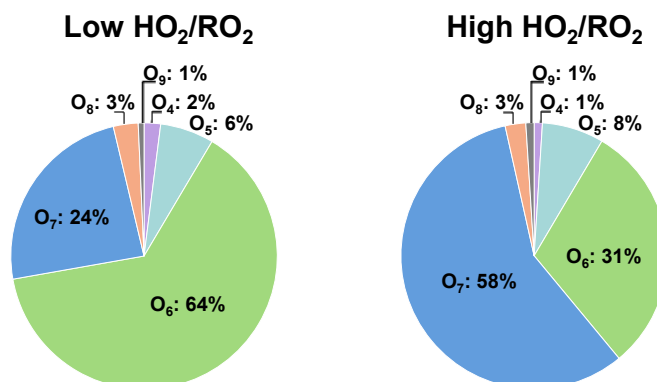
### 533 3.3 Impact on carbonyl and hydroperoxide formation

534 Increased  $\text{HO}_2/\text{RO}_2$  should shift the product distribution by reduction of alcohol and carbonyl compounds from the so-called  
535 molecular channel in the  $\text{RO}_2+\text{RO}_2$  reaction (see reaction (**R3**)), in favor of hydroperoxide formation from  $\text{RO}_2+\text{HO}_2$   
536 termination (reaction (**RI**)). This effect can be best observed in the  $\text{C}_{10}\text{H}_{18}\text{O}_z$  family, which contains the hydroperoxide and  
537 alcohol termination products arising from  $\text{C}_{10}\text{H}_{17}\text{O}_x$ .  $\text{C}_{10}\text{H}_{18}\text{O}_z$  significantly increased to on average 159 % (see **Fig. 6**). This  
538 supports an increased hydroperoxide formation, however, with some uncertainty due to the alcohol termination products  
539 from  $\text{C}_{10}\text{H}_{17}\text{O}_x$  (by reaction with  $\text{RO}_2$ ). To elucidate this further the contribution of individual species to the  $\text{C}_{10}\text{H}_{18}\text{O}_z$  family  
540 was examined.

541 Formation of an alcohol via the molecular path (reaction (**R3**)) leads to the loss of one oxygen atom compared to the  
542 precursor  $\text{C}_{10}\text{H}_{17}\text{O}_x$  radical, while in the hydroperoxide formation (reaction (**RI**)) the oxygen number remains the same. The  
543 most abundant member of the  $\text{C}_{10}\text{H}_{17}\text{O}_x$  family was  $\text{C}_{10}\text{H}_{17}\text{O}_7$  with a contribution of 72 %  $\pm$ 6 % at low  $\text{HO}_2/\text{RO}_2$ , and a  
544 contribution of 82 %  $\pm$ 1 % at high  $\text{HO}_2/\text{RO}_2$ .  $\text{C}_{10}\text{H}_{17}\text{O}_7$  terminates to  $\text{C}_{10}\text{H}_{18}\text{O}_z$  products either as an alcohol with sum  
545 formula  $\text{C}_{10}\text{H}_{18}\text{O}_6$ , or as a hydroperoxide with sum formula  $\text{C}_{10}\text{H}_{18}\text{O}_7$ . These products have additional sources from  $\text{C}_{10}\text{H}_{17}\text{O}_6$   
546 and  $\text{C}_{10}\text{H}_{17}\text{O}_8$  but due to the dominant contribution of  $\text{C}_{10}\text{H}_{17}\text{O}_7$  to the  $\text{C}_{10}\text{H}_{17}\text{O}_x$  family we expect any other production  
547 channels to be of minor importance.

548 **Figure 10** shows the HOM product distribution within the  $\text{C}_{10}\text{H}_{18}\text{O}_z$  family at low and high  $\text{HO}_2/\text{RO}_2$ . The sum of the  $\text{O}_6$  and  
549  $\text{O}_7$  product did not change significantly in the two regimes (about 88 %), showing that these are the major products, and  
550 agreeing well with the observation of  $\text{C}_{10}\text{H}_{17}\text{O}_7$  being the major  $\text{C}_{10}\text{H}_{17}\text{O}_x$  HOM- $\text{RO}_2$ . At low  $\text{HO}_2/\text{RO}_2$  the  $\text{O}_6$  product has a  
551 larger contribution of 64 %  $\pm$ 8 %, while at high  $\text{HO}_2/\text{RO}_2$  ~30% of signal is shifted to the  $\text{O}_7$  product. This shows that the  
552 increase in the  $\text{C}_{10}\text{H}_{18}\text{O}_z$  is matched with an increase of hydroperoxide formation.



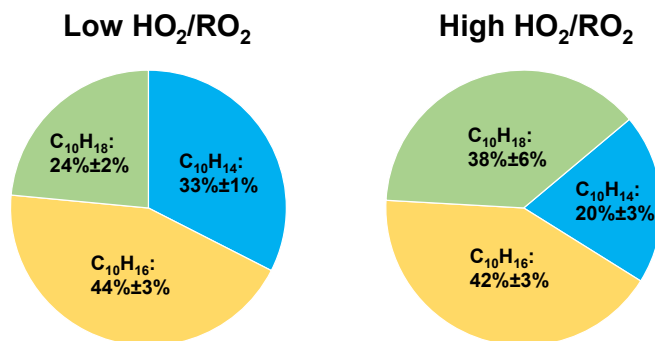


553

554 **Figure 10: Average contribution of the individual compounds to the C<sub>10</sub>H<sub>18</sub>O<sub>z</sub> family signal at low and high HO<sub>2</sub>/RO<sub>2</sub> (pure gas**  
 555 **phase experiments).**

556 An indicator for carbonyl formation is the C<sub>10</sub>H<sub>14</sub>O<sub>z</sub> family as it only contains the carbonyl products arising from  
 557 C<sub>10</sub>H<sub>15</sub>O<sub>x</sub>-RO<sub>2</sub>. The C<sub>10</sub>H<sub>14</sub>O<sub>z</sub> family was reduced on average to 61 % at high HO<sub>2</sub>/RO<sub>2</sub>, however this decrease matches the  
 558 decrease in the C<sub>10</sub>H<sub>15</sub>O<sub>x</sub> precursor family. If the reaction of a C<sub>10</sub>H<sub>15</sub>O<sub>x</sub>-HOM-RO<sub>2</sub> with a second RO<sub>2</sub> were the main  
 559 formation pathway for C<sub>10</sub>H<sub>14</sub>O<sub>z</sub> a stronger reduction would be expected as both precursor species were decreased  
 560 significantly. Instead, it appears that C<sub>10</sub>H<sub>14</sub>O<sub>z</sub> is mainly impacted by the decrease in C<sub>10</sub>H<sub>15</sub>O<sub>x</sub> as their reductions are similar.  
 561 A possible explanation could be that intramolecular termination is a major reaction pathway for C<sub>10</sub>H<sub>15</sub>O<sub>x</sub>-RO<sub>2</sub>, forming  
 562 C<sub>10</sub>H<sub>14</sub>O<sub>x</sub>-carbonyls. Intramolecular termination of the autoxidation chain has been discussed in the literature for different  
 563 VOCs (Shen et al., 2021; Guo et al., 2022), Rissanen et al. (2014) discussed the possible importance of the unimolecular  
 564 termination via an H-shift, followed by formation of a carbonyl functional group and OH loss in the autoxidation chain of  
 565 cyclohexene. Piletic and Kleindienst (2022) calculated fast reaction rate constants in the range of 1-30 s<sup>-1</sup> for such  
 566 intramolecular termination reactions to carbonyls for some C<sub>10</sub>H<sub>17</sub>O<sub>5</sub> in the α-pinene photooxidation, indicating that this  
 567 pathway could also be significant for C<sub>10</sub>H<sub>15</sub>O<sub>x</sub>. However, more investigation is necessary.

568 The overall contributions of the C<sub>10</sub>H<sub>14</sub>O<sub>z</sub>, C<sub>10</sub>H<sub>16</sub>O<sub>z</sub>, and C<sub>10</sub>H<sub>18</sub>O<sub>z</sub> families to the HOM-Mon class at high HO<sub>2</sub>/RO<sub>2</sub> are  
 569 shifted as shown in **Fig. 11**.



570

571 **Figure 11: Average contribution of the  $C_{10}H_{14}O_z$ ,  $C_{10}H_{16}O_z$ , and  $C_{10}H_{18}O_z$  family to the monomer class signal at low and high**  
 572  **$HO_2/RO_2$  (pure gas phase experiments).**

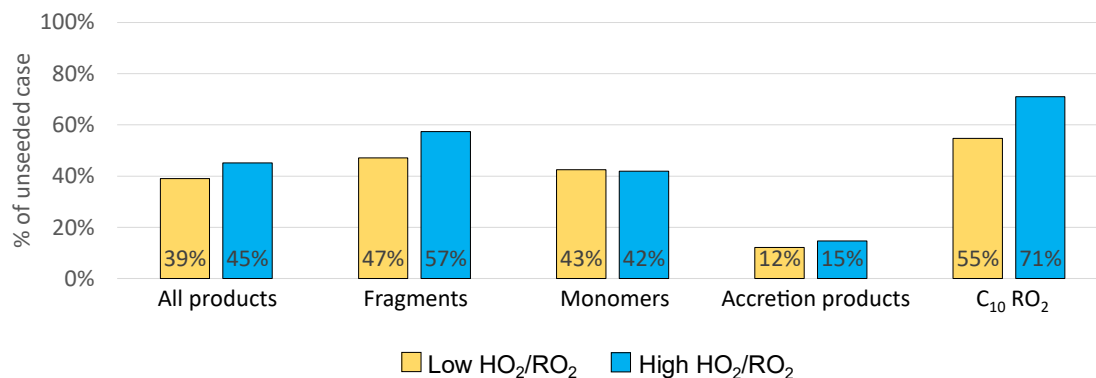
573 The contribution of  $C_{10}H_{16}O_z$  is largest and remains similar in both cases, matching the already shown unchanged signal  
 574 level in **Fig. 6**. This is the case because the  $C_{10}H_{16}O_z$  family contains the alcohols from  $C_{10}H_{15}O_x+RO_2$ , carbonyls from  
 575  $C_{10}H_{17}O_x+RO_2$  and hydroperoxides from  $C_{10}H_{15}O_x+HO_2$  (see **Fig. 1**). A separation of the effects of enhanced  $HO_2$  on this  
 576 monomer family is difficult, as for the case where  $RO_2$  termination dominates vs. the case where  $HO_2$  termination dominates,  
 577 the loss of carbonyls and alcohols is partially compensated by the gain of hydroperoxides. A strong gain in hydroperoxides is  
 578 clearly reflected in the strong increase of  $C_{10}H_{18}O_z$  at high  $HO_2/RO_2$ .

579 Inspection of the  $C_{10}H_{14}O_z$  and  $C_{10}H_{18}O_z$  families shows that ~13 % of the contribution by  $C_{10}H_{14}O_z$  are lost (carbonyls,  
 580 33 % at low  $HO_2/RO_2$ ) and are present instead as  $C_{10}H_{18}O_z$  (hydroperoxides), giving  $C_{10}H_{18}O_z$  a contribution of 38 % at high  
 581  $HO_2/RO_2$ .

### 582 3.4 Impact on condensable organic mass

583 In the previous sections we demonstrated a shift of the product distribution by the shift from low to high  $HO_2/RO_2$   
 584 conditions. We also showed that the changes could be rationalized by generic mechanistic considerations. We added  
 585  $(NH_4)_2SO_4$  seed aerosol in two experiments to determine how the shift in the product distribution affects the condensable  
 586 organic mass by determining the fraction which remained in the gas-phase after seeding.

587 **Figure 12** shows the fraction remaining for the sum of all products as well as for the individual product classes for the high  
 588 and the low  $HO_2/RO_2$  case. In both cases a significant reduction of products in the gas phase was observed with seed present.  
 589 Overall, the sum of all products was reduced by around 60 %, with a slightly higher reduction in the low  $HO_2/RO_2$  case. This  
 590 can be attributed to the larger importance of HOM-Acc in the low  $HO_2/RO_2$  case, as well as to a 10 % lower reduction of the  
 591 HOM-Frag in the high  $HO_2/RO_2$  case. In both cases a reduction of the HOM- $RO_2$  is observed, which indicates that the  
 592 provided particle sink could have affected HOM formation chemistry, however only moderately.



593

594 **Figure 12: Overview of average, relative change in product classes signal between gas phase only and seeded system. Blue shows**  
 595 **the high HO<sub>2</sub>/RO<sub>2</sub> case, yellow the low HO<sub>2</sub>/RO<sub>2</sub> case. (All are normalized to  $\alpha$ -pinene OH turnover, *Exp2* experiment)**

596 The total organic particulate mass was determined by AMS measurements and was 2.0  $\mu\text{g m}^{-3}$  and 3.4  $\mu\text{g m}^{-3}$  at high and low  
 597 HO<sub>2</sub>/RO<sub>2</sub> in the experiment (*Exp2*) displayed in **Fig. 12**. A reduction of condensed organic mass to 73 % $\pm$ 3 % at high  
 598 HO<sub>2</sub>/RO<sub>2</sub> (orange bar in **Fig. 14**) was observed on average. Since non-seeded and seeded experiments were conducted at  
 599 otherwise the same conditions and we did not observe significant new particle formation, the gas-phase compositions can be  
 600 directly compared. Therefore, we conclude that the shift in the product distribution led to a reduction of condensable material  
 601 at the same  $\alpha$ -pinene turnover with OH (and O<sub>3</sub>).

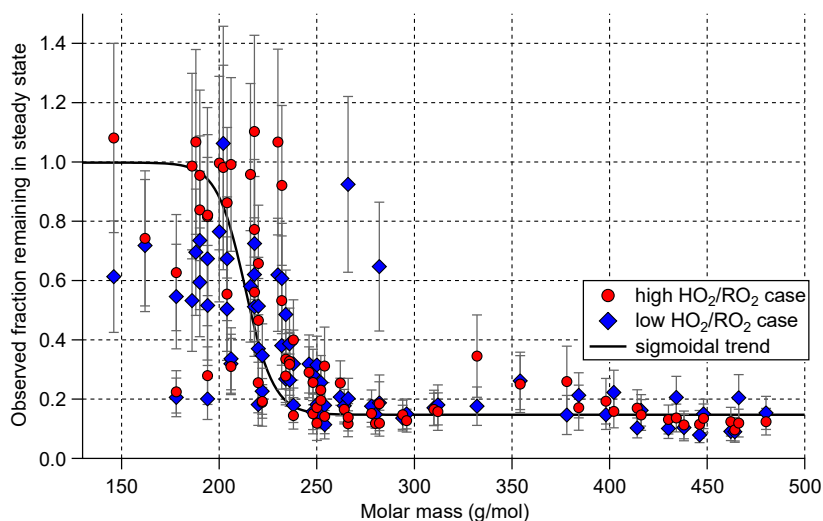
602 We calculated the wall loss corrected SOA yields with the corrected SOA mass as shown in **Eq. (4)** and as described by  
 603 Sarrafzadeh et al. (2016). To this end we used C<sub>10</sub>H<sub>16</sub>O<sub>7</sub> as the lead HOM compound. In the two experiments with seed  
 604 present (*Exp2.1* and *Exp3*) we had SOA yields of 7.3 % and 10.0 % at high HO<sub>2</sub>/RO<sub>2</sub> and 10.0 % and 12.8 % at low  
 605 HO<sub>2</sub>/RO<sub>2</sub>. The difference in the SOA yields between experiments can be explained by the slightly different OH  
 606 concentrations and subsequent difference in contribution by photooxidation (see **Table 1**). Overall, our yields are in the  
 607 lower range in comparison with the SOA yields reported by McFiggans et al. (2019) for the  $\alpha$ -pinene photooxidation.  
 608 However, our experiments were also performed at 5 °C higher temperature (20 °C compared to 15 °C in McFiggans et al.  
 609 (2019)). The SOA yields show an absolute reduction of ~3 % at high HO<sub>2</sub>/RO<sub>2</sub> compared to low HO<sub>2</sub>/RO<sub>2</sub> (relative a  
 610 reduction of about 30%). A reduction of the SOA yield of  $\alpha$ -pinene by addition of CO was described before by McFiggans et  
 611 al. (2019), however, there the  $\alpha$ -pinene OH turnover was not held constant.

612 The change from low to high HO<sub>2</sub>/RO<sub>2</sub> regime favored termination reactions to protic termination groups, as we observed  
 613 less carbonyl compounds and more hydroperoxides. This could overall shift the product distribution to products with lower  
 614 vapor pressures and favor SOA formation, since protic groups can act as hydrogen bond donors as well as hydrogen bond  
 615 acceptors. (as exemplified by the comparison of ethanol (boiling point (b.p) 78 °C) and ethane hydroperoxide (b.p. 93-97 °C)  
 616 with acetaldehyde (b.p. 20 °C) (Richter et al., 1955)). However, the effect of the termination group should be small for HOM  
 617 as they likely contain multiple hydroperoxide groups (compare Pullinen et al. (2020)). The reduction in HOM-Acc is



618 expected to decrease the condensable mass, since the HOM-Acc scavenge non-HOM-RO<sub>2</sub>, that would otherwise not partition  
619 into the particle phase.

620 Which of the measured compounds contribute significantly to the organic particle mass can be inferred by comparing their  
621 signal from the pure gas phase cases to their signal with seed in the system. Under the assumptions that, for most HOM-  
622 compounds re-evaporation to the gas phase is negligible and that the precursor chemistry is not substantially disturbed by  
623 seed addition, the fraction of signal remaining with seed in the system reflects to which degree the compound is condensing.  
624 **Figure 13** shows the fraction remaining with seed in the system plotted against the molar mass of each individual compound.  
625 The plot includes all closed shell products that were measured with a relative standard deviation of less than 30% for all  
626 measurement phases and depicts the results for both the high and low HO<sub>2</sub>/RO<sub>2</sub> case.



627

628 **Figure 13: Gas-phase fraction remaining in presence of seed (normalization of all data with  $\alpha$ -pinene OH turnover) for the low**  
629 **(blue) and high (red) HO<sub>2</sub>/RO<sub>2</sub> case. Displayed points represent all closed-shell compounds that were detected with relative**  
630 **standard deviation <30 % in all four experiment phases. Error bars represent result of error propagation (see supplement**  
631 **Sect. S7)**

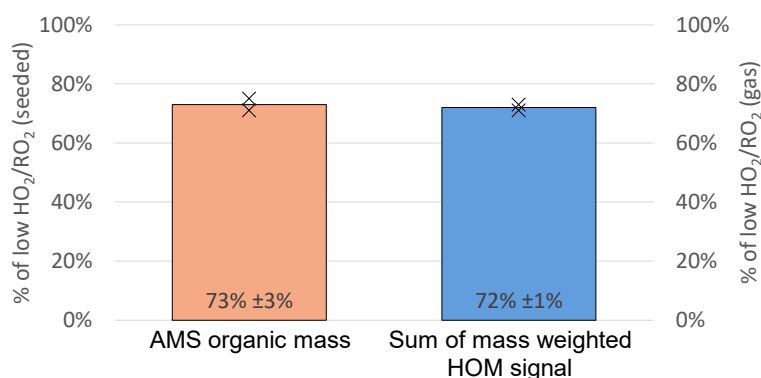
632 Overall, in both cases we observed the same trend. Lighter compounds are not affected by the presence of seed particles, but  
633 with increasing molar mass the fraction remaining in the gas phase is reduced. A difference between the low and high  
634 HO<sub>2</sub>/RO<sub>2</sub> case can be observed in the low molar mass range: In the high HO<sub>2</sub>/RO<sub>2</sub> case many fragmentation products show a  
635 higher gas-phase fraction remaining up to 1. (In some cases, values larger than 1 were observed, however within the error  
636 limits. For the error estimation see supplement Sect. S7). Fractions remaining larger than 1 beyond error could be an  
637 indication that such products have a particle-phase production source. **Figure 13** also shows a critical SVOC/LVOC region  
638 for molar masses between 175 g mol<sup>-1</sup> and 250 g mol<sup>-1</sup> where neither a fraction remaining of 1 nor complete condensation is  
639 observed. The position of this region on the molar mass scale depends on the provided organic mass concentration. The large  
640 variation of the fraction remaining in this small range of molar masses shows that the partitioning coefficients are dependent



641 on the detailed structure of the compounds and not simply on their molar mass. The semi-volatile and low volatility products  
642 represent mainly higher oxidized fragments and HOM-Mon with less than 8 oxygen.

643 For compounds with a molar mass larger than  $250 \text{ g mol}^{-1}$  a constant fraction remaining is reached in steady state, which is  
644 due to an ongoing production of the compounds. From the condensation behavior shown in **Fig. 13** we conclude that the  
645 compounds heavier than  $230 \text{ g mol}^{-1}$  are expected to be of sufficiently low volatility to be mainly found in the particle phase  
646 for the organic mass present in the system and therefore contribute significantly to the SOA mass formation. Our finding  
647 agrees with the threshold used for low volatility HOM products in Pullinen et al. (2020).

648 Therefore, the signal of all compounds with a molar mass heavier than  $230 \text{ g mol}^{-1}$  was weighted with their molar mass and  
649 summed (see **Eq. (2)**). The ratio of this weighted signal sum at low and high  $\text{HO}_2/\text{RO}_2$  is then a measure of expected SOA  
650 mass loss. The calculation leads to an expected reduction of 72 % (blue bar, **Fig. 14**). This simplified approach leads to a  
651 good agreement with the AMS measurements and can thus explain the reduced particulate organic mass within the errors.



652

653 **Figure 14: Overview of the average, relative change in organic mass observed in the AMS (left y-axis, seeded experiments) and the**  
654 **mass weighted HOM signal observed in the  $\text{NO}_3$ -CIMS (right y-axis, pure gas phase experiments) between the low and high**  
655  **$\text{HO}_2/\text{RO}_2$  case (both normalized to  $\alpha$ -pinene OH turnover).**

656 To test for closure between HOM lost and particulate organic mass measured we approximated the upper limit of HOM  
657 concentration in the condensed phase. For this calculation we used the calibration factor determined for sulfuric acid for our  
658  $\text{NO}_3$ -MION-CIMS ( $7.0 \cdot 10^9 \text{ molecules} \cdot \text{cm}^{-3} \cdot \text{ncps}^{-1}$ ) and the relationship between gas and particulate concentration of a  
659 compound in the SAPHIR STAR chamber described in **Eq. (3)**. Again, we considered all compounds with  $M > 230 \text{ g mol}^{-1}$  in  
660 our calculation. The summed mass concentration lost from the gas phase was then compared to the SOA mass measured in  
661 the AMS. This comparison yields a good agreement within the uncertainties. The detailed calculation results can be found in  
662 the supplement (**Fig. S3**). Overall, an agreement within 40 % is achieved for all measurement stages.



663 The comparisons presented above show that we understand the processes governing the SOA formation in our chamber and  
664 that the  $\text{NO}_3$ -CIMS measurements are well suited to observe the critical changes to understand the reduction in condensable  
665 organic material when shifting from low to high  $\text{HO}_2/\text{RO}_2$ .

#### 666 4 Conclusion

667 In the presented series of experiments, we achieved a shift from a  $\text{RO}_2+\text{RO}_2$  dominated chemistry to a more atmospherically  
668 relevant  $\text{HO}_2/\text{RO}_2$  ratio under constant  $\alpha$ -pinene OH turnover. It was shown that moving towards atmospheric  $\text{HO}_2/\text{RO}_2$  ratio  
669 affected the SOA formation potential, with the observed organic mass being reduced at high  $\text{HO}_2/\text{RO}_2$ . This is in support of  
670 the potential bias towards high SOA yields in chamber studies at low  $\text{HO}_2/\text{RO}_2$  as discussed by Schervish and Donahue  
671 (2021). The gas-phase observations showed that the SOA reduction at high  $\text{HO}_2/\text{RO}_2$  was mainly due to a reduced  
672 HOM-Acc formation which were formed by  $\text{RO}_2+\text{RO}_2$  cross reactions in the low  $\text{HO}_2/\text{RO}_2$  cases. This prevented  
673 contribution to SOA by less oxidized  $\text{RO}_2$  which were scavenged in the HOM-Acc at low  $\text{HO}_2/\text{RO}_2$ . Under atmospheric  
674 condition such cross reactions are less important, and such (mixed) accretion products would contribute less to SOA.

675 The overall observed HOM-products were reduced slightly, showing that under certain circumstances  $\text{RO}_2+\text{HO}_2$  termination  
676 can impede the HOM formation, mainly by reducing the precursor  $\text{RO}_2$  levels and less by impeding the autoxidation itself.  
677 The autoxidation chain (once initiated) runs to a similar oxidation level at both high and low  $\text{HO}_2/\text{RO}_2$ . The observed  
678 HOM-Mon products shift significantly between monomer families due to the different termination reaction. A decrease in  
679 carbonyl and alcohol formation from  $\text{RO}_2+\text{RO}_2$  and an increase in hydroperoxide formation from  $\text{RO}_2+\text{HO}_2$  was observed at  
680 high  $\text{HO}_2/\text{RO}_2$ .

681 Furthermore, a reduction in HOM-Frag products, especially with lower carbon numbers, as well as the parity of the  $\text{C}_{10}\text{H}_{15}\text{O}_x$   
682 HOM- $\text{RO}_2$  show a reduction in alkoxy radical formation at high  $\text{HO}_2/\text{RO}_2$ . The moderate reduction in larger HOM-Frag  
683 products and pinonaldehyde, however, suggest that some alkoxy radical steps are still important. This raises the question of  
684 whether alkoxy radical formation can be facilitated by  $\text{HO}_2$ . In the atmosphere such effects are most often overcome  
685 whenever  $\text{RO}_2+\text{NO}$  is the major alkoxy radical source.

686 Overall, the observed changes in the gas phase could be well explained with the presented generic mechanistic understanding  
687 of HOM formation in the  $\alpha$ -pinene system. The addition of seed demonstrated that the shift towards high  $\text{HO}_2/\text{RO}_2$  reduced  
688 the condensable organic mass, stressing the importance of controlling higher order reactions of peroxy radicals which lead to  
689 overemphasis of HOM-Acc product formation at low  $\text{HO}_2/\text{RO}_2$  ratios.

690 Furthermore, the seed addition allowed us to determine which products were contributing to the SOA formation and show  
691 that their volatility is a function of molar mass and detailed molecular structure. This revealed a critical mass region in which  
692 compounds have significant fractions in gas and particulate phase. Based on absorptive partitioning theory the volatilities at  
693 which this critical region is found should depend on the organic mass present in the system.



694 Valuable insight about the condensed phase can be gained from HOM gas phase measurements. We inferred conclusions  
695 about the particulate phase from the gas phase measurements and compared them to the direct particle phase observations,  
696 finding good agreements between our expectations and the measurements.

697 **Data availability**

698 All presented data will be available in a repository before the submission of the final manuscript.

699 **Author contribution**

700 TFM, MH and GM conceptualized the study and TFM, YB, SK and SRZ designed the experiments and developed the  
701 analysis methodology. The experiments were performed by YB, SK, VG and SRZ. Instrument deployment and/or data  
702 analysis were performed by YB, SK, HW, RW, JX, AZ, QH, TZ and VG. YB did model calculations of the experiments.  
703 AV, SPO, TJB, MG and MH provided counsel on experiment design and data interpretation. The compiled data set was  
704 interpreted by YB and TFM, and the results were discussed by all co-authors. YB visualized the data and YB and TFM  
705 prepared the manuscript. All co-authors reviewed the manuscript.

706 **Competing interests**

707 The authors declare that they have no conflict of interest.

708 **Financial support**

709 This research has received funding from the European Union's Horizon 2020 research and innovation programme under the  
710 FORCeS grant agreement No 821205, the Federal Ministry of Education and Research (BMBF) Germany under the FONA  
711 Strategy "Research for Sustainability" as part of the implementation of ACTRIS-D under the funding code 01LK200010,  
712 Vetenskapsrådet (VR, grant agreement No. 2018-04430), Svenska Forskningsrådet Formas (grant agreement No. 2019-586)  
713 and the Natural Environment Research Council (NERC) UK under the grant agreement No. NE/V012665/1.





## 714 References

- 715 Albrecht, S. R., Novelli, A., Hofzumahaus, A., Kang, S., Baker, Y., Mentel, T., Wahner, A., and Fuchs, H.: Measurements of  
716 hydroperoxy radicals (HO<sub>2</sub>) at atmospheric concentrations using bromide chemical ionisation mass spectrometry, *Atmos.*  
717 *Meas. Tech.*, 12, 891-902, <https://doi.org/10.5194/amt-12-891-2019>, 2019.
- 718 Atkinson, R. and Arey, J.: Atmospheric degradation of volatile organic compounds, *Chem. Rev.*, 103, 4605-4638,  
719 <https://doi.org/10.1021/cr0206420>, 2003.
- 720 Berndt, T.: Peroxy Radical Processes and Product Formation in the OH Radical-Initiated Oxidation of  $\alpha$ -Pinene for Near-  
721 Atmospheric Conditions, *J. Phys. Chem. A*, 125, 9151-9160, <https://doi.org/10.1021/acs.jpca.1c05576>, 2021.
- 722 Berndt, T., Mentler, B., Scholz, W., Fischer, L., Herrmann, H., Kulmala, M., and Hansel, A.: Accretion product formation  
723 from ozonolysis and OH radical reaction of  $\alpha$ -pinene: mechanistic insight and the influence of isoprene and ethylene,  
724 *Environ. Sci. Technol.*, 52, 11069-11077, <https://doi.org/10.1021/acs.est.8b02210>, 2018.
- 725 Berndt, T., Richters, S., Jokinen, T., Hyttinen, N., Kurtén, T., Otkjaer, R. V., Kjaergaard, H. G., Stratmann, F., Herrmann,  
726 H., Sipila, M., Kulmala, M., and Ehn, M.: Hydroxyl radical-induced formation of highly oxidized organic compounds, *Nat.*  
727 *Commun.*, 7, 13677, <https://doi.org/10.1038/ncomms13677>, 2016.
- 728 Bianchi, F., Garmash, O., He, X. C., Yan, C., Iyer, S., Rosendahl, I., Xu, Z. N., Rissanen, M. P., Riva, M., Taipale, R.,  
729 Sarnela, N., Petäjä, T., Worsnop, D. R., Kulmala, M., Ehn, M., and Junninen, H.: The role of highly oxygenated molecules  
730 (HOMs) in determining the composition of ambient ions in the boreal forest, *Atmos. Chem. Phys.*, 17, 13819-13831,  
731 <https://doi.org/10.5194/acp-17-13819-2017>, 2017.
- 732 Bianchi, F., Kurtén, T., Riva, M., Mohr, C., Rissanen, M. P., Roldin, P., Berndt, T., Crouse, J. D., Wennberg, P. O., Mentel,  
733 T. F., Wildt, J., Junninen, H., Jokinen, T., Kulmala, M., Worsnop, D. R., Thornton, J. A., Donahue, N., Kjaergaard, H. G.,  
734 and Ehn, M.: Highly Oxygenated Organic Molecules (HOM) from Gas-Phase Autoxidation Involving Peroxy Radicals: A  
735 Key Contributor to Atmospheric Aerosol, *Chem. Rev.*, 119, 3472-3509, <https://doi.org/10.1021/acs.chemrev.8b00395>, 2019.
- 736 Cox, R. A., Ammann, M., Crowley, J. N., Herrmann, H., Jenkin, M. E., McNeill, V. F., Mellouki, A., Troe, J., and  
737 Wallington, T. J.: Evaluated kinetic and photochemical data for atmospheric chemistry: Volume VII – Criegee intermediates,  
738 *Atmos. Chem. Phys.*, 20, 13497-13519, <https://doi.org/10.5194/acp-20-13497-2020>, 2020.
- 739 Crouse, J. D., Nielsen, L. B., Jørgensen, S., Kjaergaard, H. G., and Wennberg, P. O.: Autoxidation of organic compounds in  
740 the atmosphere, *J. Phys. Chem. Lett.*, 4, 3513-3520, <https://doi.org/10.1021/jz4019207>, 2013.
- 741 Eddingsaas, N., Loza, C., Yee, L., Seinfeld, J., and Wennberg, P.:  $\alpha$ -Pinene photooxidation under controlled chemical  
742 conditions – Part 1: Gas-phase composition in low- and high-NO<sub>x</sub> environments, *Atmos. Chem. Phys.*, 12, 6489-6504,  
743 <https://doi.org/10.5194/acp-12-6489-2012>, 2012.
- 744 Ehn, M., Thornton, J. A., Kleist, E., Sipila, M., Junninen, H., Pullinen, I., Springer, M., Rubach, F., Tillmann, R., Lee, B.,  
745 Lopez-Hilfiker, F., Andres, S., Acir, I. H., Rissanen, M., Jokinen, T., Schobesberger, S., Kangasluoma, J., Kontkanen, J.,  
746 Nieminen, T., Kurtén, T., Nielsen, L. B., Jørgensen, S., Kjaergaard, H. G., Canagaratna, M., Maso, M. D., Berndt, T., Petaja,  
747 T., Wahner, A., Kerminen, V. M., Kulmala, M., Worsnop, D. R., Wildt, J., and Mentel, T. F.: A large source of low-  
748 volatility secondary organic aerosol, *Nature*, 506, 476-479, <https://doi.org/10.1038/nature13032>, 2014.
- 749 Eisele, F. and Tanner, D.: Measurement of the gas phase concentration of H<sub>2</sub>SO<sub>4</sub> and methane sulfonic acid and estimates of  
750 H<sub>2</sub>SO<sub>4</sub> production and loss in the atmosphere, *J. Geophys. Res. Atmos.*, 98, 9001-9010, <https://doi.org/10.1029/93JD00031>,  
751 1993.
- 752 Fantechi, G., Vereecken, L., and Peeters, J.: The OH-initiated atmospheric oxidation of pinonaldehyde: Detailed theoretical  
753 study and mechanism construction, *Phys. Chem. Chem. Phys.*, 4, 5795-5805, <https://doi.org/10.1039/B205901K>, 2002.
- 754 Guo, Y., Shen, H., Pullinen, I., Luo, H., Kang, S., Vereecken, L., Fuchs, H., Hallquist, M., Acir, I. H., Tillmann, R., Rohrer,  
755 F., Wildt, J., Kiendler-Scharr, A., Wahner, A., Zhao, D. F., and Mentel, T. F.: Identification of highly oxygenated organic  
756 molecules and their role in aerosol formation in the reaction of limonene with nitrate radical, *Atmos. Chem. Phys.*, 22,  
757 11323-11346, <https://doi.org/10.5194/acp-22-11323-2022>, 2022.
- 758 Hallquist, M., Wenger, J. C., Baltensperger, U., Rudich, Y., Simpson, D., Claeys, M., Dommen, J., Donahue, N. M., George,  
759 C., Goldstein, A. H., Hamilton, J. F., Herrmann, H., Hoffmann, T., Iinuma, Y., Jang, M., Jenkin, M. E., Jimenez, J. L.,  
760 Kiendler-Scharr, A., Maenhaut, W., McFiggans, G., Mentel, T. F., Monod, A., Prévôt, A. S. H., Seinfeld, J. H., Surratt, J. D.,  
761 Szmigielski, R., and Wildt, J.: The formation, properties and impact of secondary organic aerosol: current and emerging  
762 issues, *Atmos. Chem. Phys.*, 9, 5155-5236, <https://doi.org/10.5194/acp-9-5155-2009>, 2009.



- 763 Hantschke, L. L.: Oxidation of monoterpenes studied in atmospheric simulation chambers, Forschungszentrum Jülich  
764 GmbH, Zentralbibliothek, Verlag, 2022.
- 765 Hasson, A. S., Kuwata, K. T., Arroyo, M. C., and Petersen, E. B.: Theoretical studies of the reaction of hydroperoxy radicals  
766 (HO<sub>2</sub>) with ethyl peroxy (CH<sub>3</sub>CH<sub>2</sub>O<sub>2</sub>), acetyl peroxy (CH<sub>3</sub>C(O)O<sub>2</sub>), and acetyl peroxy (CH<sub>3</sub>C(O)CH<sub>2</sub>O<sub>2</sub>) radicals, *J.*  
767 *Photochem. Photobiol. A*, 176, 218-230, <https://doi.org/10.1016/j.jphotochem.2005.08.012>, 2005.
- 768 Henry, K. M., Lohaus, T., and Donahue, N. M.: Organic aerosol yields from  $\alpha$ -pinene oxidation: bridging the gap between  
769 first-generation yields and aging chemistry, *Environ. Sci. Technol.*, 46, 12347-12354, <https://doi.org/10.1021/es302060y>,  
770 2012.
- 771 Hidy, G.: Atmospheric chemistry in a box or a bag, *Atmos.*, 10, 401, <https://doi.org/10.3390/atmos10070401>, 2019.
- 772 Hyttinen, N., Otkjær, R. V., Iyer, S., Kjaergaard, H. G., Rissanen, M. P., Wennberg, P. O., and Kurtén, T.: Computational  
773 comparison of different reagent ions in the chemical ionization of oxidized multifunctional compounds, *J. Phys. Chem. A*,  
774 122, 269-279, <https://doi.org/10.1021/acs.jpca.7b10015>, 2018.
- 775 Iyer, S., Reiman, H., Møller, K. H., Rissanen, M. P., Kjaergaard, H. G., and Kurtén, T.: Computational investigation of  
776 RO<sub>2</sub>+ HO<sub>2</sub> and RO<sub>2</sub>+ RO<sub>2</sub> reactions of monoterpene derived first-generation peroxy radicals leading to radical recycling, *J.*  
777 *Phys. Chem. A*, 122, 9542-9552, <https://doi.org/10.1021/acs.jpca.8b09241>, 2018.
- 778 Iyer, S., Rissanen, M. P., Valiev, R., Barua, S., Krechmer, J. E., Thornton, J., Ehn, M., and Kurtén, T.: Molecular mechanism  
779 for rapid autoxidation in  $\alpha$ -pinene ozonolysis, *Nat. Commun.*, 12, 878, <https://doi.org/10.1038/s41467-021-21172-w>, 2021.
- 780 Jenkin, M. E., Saunders, S. M., and Pilling, M. J.: The tropospheric degradation of volatile organic compounds: a protocol  
781 for mechanism development, *Atmos. Environ.*, 31, 81-104, [https://doi.org/10.1016/S1352-2310\(96\)00105-7](https://doi.org/10.1016/S1352-2310(96)00105-7), 1997.
- 782 Jenkin, M. E., Valorso, R., Aumont, B., and Rickard, A. R.: Estimation of rate coefficients and branching ratios for reactions  
783 of organic peroxy radicals for use in automated mechanism construction, *Atmos. Chem. Phys.*, 19, 7691-7717,  
784 <https://doi.org/10.5194/acp-19-7691-2019>, 2019.
- 785 Johnson, D. and Marston, G.: The gas-phase ozonolysis of unsaturated volatile organic compounds in the troposphere,  
786 *Chem. Soc. Rev.*, 37, 699-716, <https://doi.org/10.1039/B704260B> 2008.
- 787 Junninen, H., Ehn, M., Petäjä, T., Luosujärvi, L., Kotiaho, T., Kostianen, R., Rohner, U., Gonin, M., Fuhrer, K., Kulmala,  
788 M., and Worsnop, D. R.: A high-resolution mass spectrometer to measure atmospheric ion composition, *Atmos. Meas.*  
789 *Tech.*, 3, 1039-1053, <https://doi.org/10.5194/amt-3-1039-2010>, 2010.
- 790 Kang, S.: Formation of highly oxygenated organic molecules from  $\alpha$ -pinene photochemistry, Forschungszentrum Jülich  
791 GmbH, 2021.
- 792 Kiendler-Scharr, A., Wildt, J., Maso, M. D., Hohaus, T., Kleist, E., Mentel, T. F., Tillmann, R., Uerlings, R., Schurr, U., and  
793 Wahner, A.: New particle formation in forests inhibited by isoprene emissions, *Nature*, 461, 381-384,  
794 <https://doi.org/10.1038/nature08292>, 2009.
- 795 McFiggans, G., Mentel, T. F., Wildt, J., Pullinen, I., Kang, S., Kleist, E., Schmitt, S., Springer, M., Tillmann, R., Wu, C.,  
796 Zhao, D., Hallquist, M., Faxon, C., Le Breton, M., Hallquist, A. M., Simpson, D., Bergstrom, R., Jenkin, M. E., Ehn, M.,  
797 Thornton, J. A., Alfarra, M. R., Bannan, T. J., Percival, C. J., Priestley, M., Topping, D., and Kiendler-Scharr, A.: Secondary  
798 organic aerosol reduced by mixture of atmospheric vapours, *Nature*, 565, 587-593, <https://doi.org/10.1038/s41586-018-0871-y>,  
799 2019.
- 800 Mentel, T., Springer, M., Ehn, M., Kleist, E., Pullinen, I., Kurtén, T., Rissanen, M., Wahner, A., and Wildt, J.: Formation of  
801 highly oxidized multifunctional compounds: autoxidation of peroxy radicals formed in the ozonolysis of alkenes—deduced  
802 from structure–product relationships, *Atmos. Chem. Phys.*, 15, 6745-6765, <https://doi.org/10.5194/acp-15-6745-2015>, 2015.
- 803 Mentel, T. F., Wildt, J., Kiendler-Scharr, A., Kleist, E., Tillmann, R., Dal Maso, M., Fisseha, R., Hohaus, T., Spahn, H.,  
804 Uerlings, R., Wegener, R., Griffiths, P. T., Dinar, E., Rudich, Y., and Wahner, A.: Photochemical production of aerosols  
805 from real plant emissions, *Atmos. Chem. Phys.*, 9, 4387-4406, <https://doi.org/10.5194/acp-9-4387-2009>, 2009.
- 806 Mohr, C., Thornton, J. A., Heitto, A., Lopez-Hilfiker, F. D., Lutz, A., Riipinen, I., Hong, J., Donahue, N. M., Hallquist, M.,  
807 Petaja, T., Kulmala, M., and Yli-Juuti, T.: Molecular identification of organic vapors driving atmospheric nanoparticle  
808 growth, *Nat. Commun.*, 10, 4442, <https://doi.org/10.1038/s41467-019-12473-2>, 2019.
- 809 Piletic, I. R. and Kleindienst, T. E.: Rates and yields of unimolecular reactions producing highly oxidized peroxy radicals in  
810 the OH-induced autoxidation of  $\alpha$ -pinene,  $\beta$ -pinene, and limonene, *J. Phys. Chem. A*, 126, 88-100,  
811 <https://doi.org/10.1021/acs.jpca.1c07961>, 2022.



- 812 Pullinen, I., Schmitt, S., Kang, S., Sarrafzadeh, M., Schlag, P., Andres, S., Kleist, E., Mentel, T. F., Rohrer, F., Springer, M.,  
813 Tillmann, R., Wildt, J., Wu, C., Zhao, D., Wahner, A., and Kiendler-Scharr, A.: Impact of NO<sub>x</sub> on secondary organic aerosol  
814 (SOA) formation from  $\alpha$ -pinene and  $\beta$ -pinene photooxidation: the role of highly oxygenated organic nitrates, *Atmos. Chem.*  
815 *Phys.*, 20, 10125-10147, <https://doi.org/10.5194/acp-20-10125-2020>, 2020.
- 816 Richter, F., Ostertag, R., Ammerlahn, G., Behrle, E., Baumann, M., and Kobel, M.: Beilstein's handbook of organic  
817 chemistry. Third supplement, covering the literature from 1930-1949, 1955.
- 818 Rissanen, M. P., Mikkilä, J., Iyer, S., and Hakala, J.: Multi-scheme chemical ionization inlet (MION) for fast switching of  
819 reagent ion chemistry in atmospheric pressure chemical ionization mass spectrometry (CIMS) applications, *Atmos. Meas.*  
820 *Tech.*, 12, 6635-6646, <https://doi.org/10.5194/amt-12-6635-2019>, 2019.
- 821 Rissanen, M. P., Kurtén, T., Sipila, M., Thornton, J. A., Kangasluoma, J., Sarnela, N., Junninen, H., Jorgensen, S.,  
822 Schallhart, S., Kajos, M. K., Taipale, R., Springer, M., Mentel, T. F., Ruuskanen, T., Petaja, T., Worsnop, D. R., Kjaergaard,  
823 H. G., and Ehn, M.: The formation of highly oxidized multifunctional products in the ozonolysis of cyclohexene, *J. Am.*  
824 *Chem. Soc.*, 136, 15596-15606, <https://doi.org/10.1021/ja507146s>, 2014.
- 825 Roldin, P., Ehn, M., Kurtén, T., Olenius, T., Rissanen, M. P., Sarnela, N., Elm, J., Rantala, P., Hao, L., Hyttinen, N.,  
826 Heikkinen, L., Worsnop, D. R., Pichelstorfer, L., Xavier, C., Clusius, P., Öström, E., Petäjä, T., Kulmala, M., Vehkamäki,  
827 H., Virtanen, A., Riipinen, I., and Boy, M.: The role of highly oxygenated organic molecules in the Boreal aerosol-cloud-  
828 climate system, *Nat. Commun.*, 10, 4370, <https://doi.org/10.1038/s41467-019-12338-8>, 2019.
- 829 Sanchez, J., Tanner, D. J., Chen, D., Huey, L. G., and Ng, N. L.: A new technique for the direct detection of HO<sub>2</sub> radicals  
830 using bromide chemical ionization mass spectrometry (Br-CIMS): initial characterization, *Atmos. Meas. Tech.*, 9, 3851-  
831 3861, <https://doi.org/10.5194/amt-9-3851-2016>, 2016.
- 832 Sarrafzadeh, M., Wildt, J., Pullinen, I., Springer, M., Kleist, E., Tillmann, R., Schmitt, S. H., Wu, C., Mentel, T. F., Zhao,  
833 D., Hastie, D. R., and Kiendler-Scharr, A.: Impact of NO<sub>x</sub> and OH on secondary organic aerosol formation from  $\beta$ -pinene  
834 photooxidation, *Atmos. Chem. Phys.*, 16, 11237-11248, <https://doi.org/10.5194/acp-16-11237-2016>, 2016.
- 835 Saunders, S. M., Jenkin, M. E., Derwent, R., and Pilling, M.: Protocol for the development of the Master Chemical  
836 Mechanism, MCM v3 (Part A): tropospheric degradation of non-aromatic volatile organic compounds, *Atmos. Chem. Phys.*,  
837 3, 161-180, <https://doi.org/10.5194/acp-3-161-2003>, 2003.
- 838 Schervish, M. and Donahue, N. M.: Peroxy radical kinetics and new particle formation, *Environ. Sci. Atmos.*, 1, 79-92,  
839 <https://doi.org/10.1039/d0ea00017e>, 2021.
- 840 Shen, H., Vereecken, L., Kang, S., Pullinen, I., Fuchs, H., Zhao, D., and Mentel, T. F.: Unexpected significance of a minor  
841 reaction pathway in daytime formation of biogenic highly oxygenated organic compounds, *Sci. Adv.*, 8, eabp8702,  
842 <https://doi.org/10.1126/sciadv.abp8702>, 2022.
- 843 Shen, H., Zhao, D., Pullinen, I., Kang, S., Vereecken, L., Fuchs, H., Acir, I. H., Tillmann, R., Rohrer, F., Wildt, J., Kiendler-  
844 Scharr, A., Wahner, A., and Mentel, T. F.: Highly Oxygenated Organic Nitrates Formed from NO(3) Radical-Initiated  
845 Oxidation of  $\beta$ -Pinene, *Environ. Sci. Technol.*, 55, 15658-15671, <https://doi.org/10.1021/acs.est.1c03978>, 2021.
- 846 Shilling, J. E., Chen, Q., King, S. M., Rosenoern, T., Kroll, J. H., Worsnop, D. R., DeCarlo, P. F., Aiken, A. C., Sueper, D.,  
847 Jimenez, J. L., and Martin, S. T.: Loading-dependent elemental composition of  $\alpha$ -pinene SOA particles, *Atmos. Chem.*  
848 *Phys.*, 9, 771-782, <https://doi.org/10.5194/acp-9-771-2009>, 2009.
- 849 Vereecken, L., Müller, J.-F., and Peeters, J.: Low-volatility poly-oxygenates in the OH-initiated atmospheric oxidation of  $\alpha$ -  
850 pinene: impact of non-traditional peroxy radical chemistry, *Phys. Chem. Chem. Phys.*, 9, 5241-5248,  
851 <https://doi.org/10.1039/b708023a>, 2007.
- 852 Wildt, J., Mentel, T. F., Kiendler-Scharr, A., Hoffmann, T., Andres, S., Ehn, M., Kleist, E., Müsgen, P., Rohrer, F., Rudich,  
853 Y., Springer, M., Tillmann, R., and Wahner, A.: Suppression of new particle formation from monoterpene oxidation by  
854 NO<sub>x</sub>, *Atmos. Chem. Phys.*, 14, 2789-2804, <https://doi.org/10.5194/acp-14-2789-2014>, 2014.
- 855 Xu, L., Møller, K. H., Crouse, J. D., Otkjær, R. V., Kjaergaard, H. G., and Wennberg, P. O.: Unimolecular reactions of  
856 peroxy radicals formed in the oxidation of  $\alpha$ -pinene and  $\beta$ -pinene by hydroxyl radicals, *J. Phys. Chem. A*, 123, 1661-1674,  
857 <https://doi.org/10.1021/acs.jpca.8b11726>, 2019.
- 858